Climate Dynamics (2006)
DOI 10.1007/s00382-006-0141-9

Leonard M. Druyan · Matthew Fulakeza
Patrick Lonergan

Mesoscale analyses of West African summer climate: focus on wave disturbances

Received: 5 April 2005 / Accepted: 9 March 2006

Abstract A mesoscale climate data set is created from simulations with a regional (limited area) model over West Africa on a 0.5° grid, covering six summers (June–September), 1998–2003. The Regional Model 3 (RM3) is the latest version run at the National Aeronautics and Space Administration Goddard Institute for Space Studies and the (Columbia University) Center for Climate Systems Research. RM3 simulations are driven by synchronous lateral boundary data four times daily from the National Center for Environmental Prediction reanalysis (NCPR) on a 2.5° grid and sea-surface temperatures from the reanalysis. Characteristics of African wave disturbances (AWD) are analyzed from the mesoscale data set and compared to prior published descriptions. Results show a remarkably high correlation in time and space between RM3 modeled precipitation and Tropical Rainfall Measurement Mission daily estimates, although the RM3 underestimates the frequency of the most extreme (high and low) precipitation rates. In addition, regional model precipitation was validated against gridded seasonal means from the East Anglia University data set and against a time series of daily rain gauge observations near Niamey, Niger. RM3 700 mb circulation shows evidence of considerable interannual variability in spectral properties that relate to AWD. Spectral amplitudes for 700 mb meridional wind time series peak most often in the range of 4 to 6-day periods over swaths traversed by AWD, often detected along 17°N and 4°N. AWD also create westward propagating bands of alternating southerlies and northerlies in NCPR, European Center for Medium-range Weather Forecasting 40-year reanalysis (ERA-40) and RM3 700 mb circulations. RM3 700 mb meridional winds are highly correlated with corresponding NCPR and ERA-40 values, but are usually weaker, so RM3 AWD generally have lower amplitudes. Significant rain events are not always associated with AWD. The RM3 shows good potential for sensitivity experiments that will contribute to our understanding of the physical mechanisms underlying the variability of the West African monsoon. An RM3 West Africa mesoscale climatology could also prove useful for future climate research.

L. M. Druyan (✉) · M. Fulakeza · P. Lonergan
NASA/Goddard Institute for Space Studies,
2880 Broadway, New York, NY 10025, USA
E-mail: LDruyan@giss.nasa.gov

L. M. Druyan · M. Fulakeza
Center for Climate Systems Research,
Earth Institute at Columbia University,
2880 Broadway, New York, NY 10025, USA

P. Lonergan
Stinger Ghaffarian Technology, Inc.,
2880 Broadway, New York, NY 10025, USA

1 Introduction

Given the serious socio-economic impact of periodic droughts on the fragile agriculturally based societies of West Africa's Sahel, it is desirable to improve our understanding of the region's climate variability, especially rainfall variability. Ultimately, seasonal predictions relating to the summer monsoon would be beneficial. Better understanding requires more modeling studies and more empirical investigations. The sparse distribution of meteorological stations throughout West Africa encourages the exploitation of gridded data sets from reanalyses for which internally consistent three-dimensional interpolation has somewhat compensated for the paucity of observational data. Archived NCEP reanalysis (Kistler et al. 2001) and ECMWF reanalysis (Gibson et al. 1997; Uppala et al. 2005) data sets have been created by global spectral model assimilations of observational data at equivalent grid spacings of about 210 and 125 km, respectively, updated four times per day and archived on 2.5° grids. However, the spatial scales of important weather-making systems, such as squall lines and African wave disturbances (AWD), may require higher resolution (Druyan et al. 1997). This paper describes a climate data set for West Africa, for June–September in each of the years 1998–2003, that has been simulated by a regional, limited area model (LAM) on a 0.5° latitude by longitude grid. Lateral boundary conditions (LBCs) to drive the LAM were taken from NCEP reanalysis (hereafter National Center for Environmental Prediction reanalysis, NCPR).

Dynamic downscaling a reanalysis with LAMs creates high horizontal resolution data sets (e.g., Leung et al. 2004). LAM simulations are not interpolations of the forcing analysis since the integration of the governing kinematic and thermodynamic equations can take advantage of more precisely defined gradients of the variables and of the terrain heights. "The fundamental hypothesis underlying the use of LAMs is their ability to generate meaningful small-scale features from low-resolution information, provided as initial conditions (De Ela et al. 2002)." However, the downscaled results can be quite different than the driving model representation or the driving analysis. Denis et al. (2002) found, in short experiments over the northeast US and southeast Canada, that small low-level features absent from low-resolution initial conditions were almost fully regenerated by the LAM within the first day. Moreover, mesoscale features of the sea-level pressure and low-level temperature distributions were simulated by the LAM quite accurately in time and space, and the time variability of precipitation was well reproduced. Whether these advantages persist for seasonal-length simulations needs to be investigated, but Denis et al. (2002) did show that lower boundary surface heterogeneities are crucial for simulating stationary mesoscale climate features.

Giorgi et al. (1993) found it "feasible to perform good quality, multiyear simulations with current LAMs and, therefore... to apply such models to climate studies." Many modeled physical processes are grid resolution dependent, most importantly advection and precipitation (Giorgi and Marinucci 1996). Leung et al. (2003) studied the hydroclimate of the western US using MM5 simulations in a double nesting (outer grid: 120 km; inner grid: 40 km) driven by NCEP reanalysis data for 1981–2000. The simulated climate on the 40-km grid reproduced many important mesoscale climate features, although the MM5 produced a warm surface air temperature bias, overestimated precipitation in the basins and intermountain west during winters and underestimated summer monsoon rainfall in the Southwest. The last was traced to insufficient precipitation frequency. There were noticeable advantages for the precipitation simulation that derived from the 40-km topography.

Transient AWD are mid-tropospheric easterly waves, and have a role in modulating the precipitation of West Africa during the summer monsoon season (Reed et al. 1977; Duvel 1990; Druyan et al. 1996). Much of the Sahel's seasonal rainfall occurs in organized squall lines (Lamb and Peppler 1991) and many of them are imbedded within AWD (Fortune 1980; Landsea and Gray 1992), so these synoptic disturbances are quite relevant to the local climate variability (Ward et al. 2004). AWD derive their energy from the vertical and horizontal shear created by the mid-tropospheric African Easterly Jet (AEJ) at 600 mb, reflecting the combined influences of baroclinic and barotropic instability (Norquist et al. 1977). Refined understanding of AWD behavior and characteristics should contribute to improved regional planning as well as to advancing the challenge of seasonal forecasting. Given the centrality of the AEJ and AWD in the evolution of the summertime climate over West Africa, models are challenged to produce realistic simulations, but high horizontal resolution is a definite asset.

Diedhiou et al. (1999) investigated the properties of AWD based on NCEP and ECMWF daily reanalysis data gridded at 2.5° by 2.5°. Their study offers power spectra of 700 mb meridional wind (*v7*) time series for which spectral peaks at 3.5–4.5 days were prominent south of 20°N over West Africa and periods of 6–9 days were evident at grid points north of that latitude. These average spectral amplitudes (ASAs), based on at least 15 years of reanalysis data, were weaker than previously analyzed values for specific seasons by Duvel (1990) and Druyan and Hall (1996) in a GCM study. Moreover, significant differences were evident in results from the NCEP versus the ECMWF data sets. In addition, rather large interannual variations occurred in the variance of 3 to 5-day period filtered meridional winds over West Africa, including a positive trend based on NCEP reanalyses. No attempt was made to relate these trends in circulation to the interannual variability of precipitation.

Both the NCEP and ECMWF reanalyses used by Diedhiou et al. (1999) to construct their multi-year AWD climatology represent meteorological variables on 2.5° by 2.5° grids, based on model simulations that resolve gradients and terrain slopes on equivalent grid intervals of about 210 and 125 km, respectively. Even with reanalysis data gridded at the same resolution, analyzed wave properties differed between the two systems, probably because of model dependence. Moreover, Diedhiou et al. (1999) reported that the lag-correlations, which were an important part of their work, required interpolation down to 0.25°, but since this was linear, horizontal gradient information was not improved. Their analysis found AWD wavelengths ranging from 3,000–5,000 km at 700 mb over West Africa. Indeed, characteristics of AWD in much of the literature have been gleaned from low spatial resolution analyses, or from empirical studies based on sparse networks of station observations covering time spans of 2 days to several years.

Druyan et al. (2000, 2001) described the first analyses of daily AWD features based on regional model simulations on the same 0.5° horizontal grid used in the present investigation. Model improvements incorporated into the latest version (hereafter RM3) have meanwhile greatly improved precipitation simulations over West Africa (Druyan and Fulakeza 2005). The current study of the RM3 June–September climate over West Africa gives particular attention to the analysis of AWD characteristics. Representation of AWD by high-resolution simulations offers distinct advantages over the products of coarser resolution global models heretofore used in AWD studies and previous results based on sparse networks of observations. The study also includes comparison of model simulated fields to empirical evidence in order to better appreciate the relevance of results to the real world. Section 4.4 describes the results of an experiment that tests the sensitivity of model simulated precipitation to the resolution of orography.

2 Methods and data

West Africa is in the center of the RM3 computational domain, which is bounded by 20°S–35°N, 35°W–35°E. RM3 simulations for the study were driven by synchronous LBCs, time interpolated from four times daily NCPR. Druyan and Fulakeza (2005) determined the need for a spin-up period of at least 1 week to allow the RM3 to adjust to NCPR initial conditions. The June–September simulations were therefore begun from NCPR atmospheric conditions, soil moisture, ground and sea-surface temperatures (SST) on May 15th of each year. Time varying NCPR SST were prescribed as the lower boundary conditions throughout the simulations. Ground temperatures and soil moisture were, however, continuously updated by the RM3. The structure of the RM3 is outlined in the following section. Data used to validate RM3 simulations are described next.

RM3 simulation results are compared to several sources of observational data:

1. The Climate Research Unit's (CRU, East Anglia University) analyses of monthly mean precipitation and surface air temperature for continental areas are based on station observations that have been interpolated to a 0.5° grid (New et al. 2002). The data sets are available up to and including the year 2000.
2. Tropical rainfall microwave measurement (TRMM) satellite estimates of daily precipitation. Druyan and Fulakeza (2005) and Huffman et al. (1997) discuss their merit. These data, from the 3B42 set are available for 1° by 1° squares between 40°N and 40°S, beginning in 1998. Daily estimates are based on a modification of the Global Precipitation Index (GPI) from geostationary satellite infrared (IR) measurements. To form the final data set, GPI values are calibrated by TRMM microwave, radar, visible and IR observations. Note that the TRMM radar and microwave observe only over a narrow swath at a single time of day, therefore taking 1–2 days to cover the entire tropics and many weeks to see the diurnal cycle at any location. Consequently, in order to make 3B-42, the combined radar-microwave estimate is taken wherever available and statistics are used to "train" an IR-only estimate of precipitation at the same place using the combined estimate. Accordingly, the 3B-42 rainfall is more an "educated (by the radar and microwave) tweaking" of the standard GPI estimate. Lau et al. (2004) compared the TRMM 3B-42 data during July 2001 to daily rain gauge measurements at two stations in the Himalayas. They found that the TRMM estimates reproduced ground observations very well, including the detection of a heavy precipitation event on 19–20 July 2001.
3. NCEP reanalysis (NCPR) data sets (Kistler et al. 2001) provide four times daily and monthly means of many climate variables at 2.5° horizontal grid resolution, based on data assimilation executed at an equivalent grid spacing of about 210 km. Although these data sets are used to drive the RM3 by providing LBCs and evolving SST, the RM3 simulated climate within the domain was never updated or nudged by NCPR. Comparison of the RM3 simulations to corresponding NCPR fields serves two purposes: to evaluate the effect of dynamic downscaling to the higher resolution and to validate the RM3 against analyses that assimilated station observations four times daily over West Africa. Data from such observations presumably did not affect RM3 simulations within the domain of the study.
4. European Center for Medium Range Weather Forecasting (ECMWF) 40-year (1957–2002) reanalysis (ERA-40) (Uppala et al. 2005) also provides three-dimensional data sets on a 2.5° latitude–longitude grid four times per day. These analyses are largely based on many of the same observations as NCPR, but their assimilation has been carried out with a different model computing on an equivalent grid of 125 km spacing. Validation of some RM3 fields against ERA-40 data provides an independent check since these data were not used to drive the RM3 simulations.
5. Daily rain gauge observations for July–September 2000 and aircraft/dropsonde wind measurements, all published by Thorncroft et al. (2003), provide an additional source for validating RM3 precipitation and circulation near Niamey.

3 The regional model

The regional model at GISS/CCSR has been previously used to study AWD (Druyan et al. 2000, 2001, 2004). It uses the primitive equations with a semi-Lagrangian advection scheme and semi-implicit time differencing at 15 vertical sigma levels. Recent work suggests that model performance can be improved by increasing the vertical resolution. For the current study, the newest third-generation version, RM3, uses the same land surface (LS) process model used in the GISS GCM (Rosenzweig and Abramopoulos 1997; Hansen et al. 2002), although some modifications have been lately introduced. TOPMODEL algorithms (Beven and Kirkby 1979) are now used to compute surface and underground runoff and more efficient code has been introduced for the computations of heat and water fluxes. The LS model consists of two integrated parts, the soil and the canopy, and it conserves water and heat while simulating their vertical fluxes. Grid elements are divided into bare and vegetated portions, each with its own set of prognostic variables. The RM3 modeled soil is divided into six layers to a depth of 3.5 m. The model distinguishes between five textures of soil: sand, loam, clay, peat and rock. Surface runoff is defined by the infiltration capacity of the upper soil layer.

The canopy, modeled as a separate layer located above the soil, is responsible for the interception of precipitation, evaporation of accumulated water and removal of soil water through transpiration. The model has six types of vegetation applicable to West Africa: grassland, shrub, woodland, deciduous, evergreen and rainforest according to Matthews (1983, 1984). Seasonal variations of leaf area index are also included. Accumulated water is evaporated from the wet canopy while the dry canopy removes water from the soil via transpiration. Transpiration depends on the canopy conductance, which in turn is determined by stomatal resistance, leaf area index, incoming radiation, canopy temperature and soil water availability.

The Del Genio and Yao (1993) moist convection parameterization and the Del Genio et al. (1996) scheme for the effects of cloud liquid water have also been incorporated into the RM3. These are components originally developed for the GISS GCM, which itself has been extensively applied to climate sensitivity studies (e.g., Hansen et al. 2002). The convection scheme incorporates entraining and non-entraining plumes, downdrafts and subsidence. Vertical cumulus mass fluxes are proportional to the moist static stability and are constrained to relax the atmosphere to a neutrally stable state at the cloud base. The convective plume and subsiding environment transport grid-scale horizontal momentum. Convective cloud cover is assigned as proportional to the mean pressure thickness of all model layers up to the cloud top.

The cloud liquid water scheme (Del Genio et al. 1996) allows for life cycle effects in stratiform clouds and permits cloud optical properties to be determined interactively. Cloud optical thickness is calculated from the predicted liquid/ice water path and a variable droplet effective radius estimated by assuming constant droplet number concentration. Microphysical and radiative properties are assumed to be different for liquid and ice clouds, and for liquid clouds over land and ocean. Mixed phase processes can change the phase if ice falls into a lower layer containing supercooled liquid water. The scheme parameterizes Bergeron–Findeisen diffusional growth of the ice phase at the expense of the liquid phase via the "seeder-feeder" process by allowing a layer with supercooled water to glaciate if sufficient ice falls into it from above.

Fritsch and Carbone (2004) noted serious deficiencies in the current technology of modeled moist convection that is used as the basis for warm-season quantitative precipitation forecasting. Nevertheless, in preliminary August simulations driven by LBCs provided four times daily from NCPR, the RM3 gave very encouraging results (Druyan and Fulakeza 2005). Simulated time–space patterns of westward-propagating precipitation swaths compared quite favorably with daily estimates from TRMM satellite data after an initial spin-up of about 6 days.

In the experiments described here, LBCs are obtained from NCPR four times daily. These externally specified field values are then merged with forecasted variables produced by the RM3 by weighting them with progressively decreasing weights inward within a buffer zone that completely surrounds the domain of interest. Optimal treatment of this approach avoids over-damping of incoming waves, but care must also be taken not to create reflections by too sharp a transition. The buffer zone consists of n grid elements and the relative weights [wt] of the LBCs vary according to the formulation:

$$\mathrm{wt} = k \times \exp(-p \times r), \tag{1}$$

where k and p are coefficients that determine the relative influence of the LBCs and r is the row number from 1 to n. For the present simulations the buffer zone consists of six grid elements ($n=6$), $k=2.2$ and $P=0.8$.

This study examines six 4-month simulations, June–September (JJAS), 1998–2003, all initialized on May 15th. These are years for which validating TRMM precipitation estimates are available.

4 Results

4.1 Validation of the mean state and the African Easterly Jet

Moustaoui et al. (2002) reported unrealistically strong monsoon westerlies over West Africa in their GCM simulations spanning 14 summers. Grist and Nicholson (2001) attribute the strength of monsoon westerlies over the Sahel to the magnitude of the cross-equatorial pressure gradient and conservation of absolute vorticity. However, Moustaoui et al. (2002) speculated that discrepancies in the simulated strength of monsoon westerlies might reflect limitations in a model's treatment of LS processes, perhaps because such limitations compromise the simulation of the distinctive meridional temperature gradient between the Sahara and the Gulf of Guinea. Druyan et al. (2004) demonstrated that too weak a temperature gradient can result in unrealistically strong near-surface westerlies, as well as a latitudinal displacement of the mid-tropospheric AEJ.

Figure 1a shows the cross-section of RM3 zonal wind speeds along 0° averaged for JJAS 1998–2003. Monsoon westerlies in the lowest layers are realistically reversed

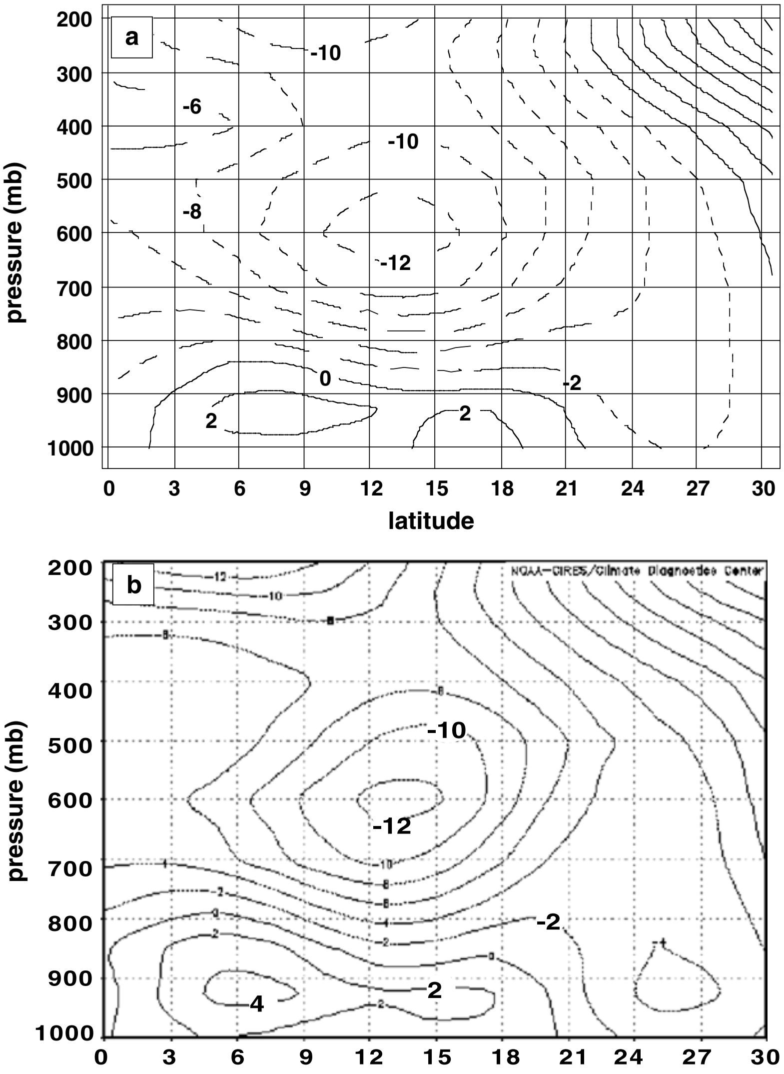

Fig. 1 Cross-section of the JJAS 1998–2003 zonal circulation (ms^{-1}) along 0° longitude: **a** RM3 and **b** NCEP reanalysis (Courtesy of Climate Diagnostics Center/NOAA)

with altitude by the vertical wind shear of the zonal circulation, creating an AEJ core of strong mid-tropospheric easterlies peaking at 600 mb over 13°N, with a core speed of almost 13 ms^{-1}. This structure resembles the corresponding NCPR cross-section (Fig. 1b) regarding AEJ core speed and location. Low-level monsoon westerlies cross the West African coast and penetrate to about 21°N during most of the summer. Figure 1 shows that these westerlies are stronger for NCPR than for the RM3 as they cross the 0° meridian. For the individual seasons of the RM3 simulations (not shown), the greatest departures from the mean state are the strong and slightly southward-displaced AEJ core (maximum speed ~14 ms^{-1}) for JJAS 2000 combined with rather weak near-surface westerlies, a weaker AEJ core (not quite 11 ms^{-1}) for JJAS 2003, and stronger 950 mb westerlies (~5 ms^{-1}) for JJAS 2002 and 2003. NCPR does not resolve the aforementioned small anomalies in AEJ core speeds computed by the RM3, but NCPR monsoon westerlies are indeed anomalously strong for JJAS 2002 and 2003, as in the model results. Both the RM3 and NCPR show that the AEJ reaches its northernmost latitude in August (not shown), before retreating in September.

Thorncroft et al. (2003) report the results of JET2000, which included detailed aircraft and dropsonde measurements of the zonal wind between 8 and 19°N, along 2.5°E on 28–29 August 2000. Figure 2 shows a cross-section of zonal wind speeds as the average of the 06 UT and 12 UT fields from the RM3 JJAS 2000 simulation on 29 August, which roughly corresponds to Fig. 11 in Thorncroft et al. (2003). While the comparison is favorable regarding the rather elongated jet core extending from 9°N to about 14°N at 650 mb, many details of the JET2000 distribution of zonal wind are not captured in Fig. 2. For example, while Fig. 2 does show the interruption of near-surface westerlies at 11°N, it does not indicate the anomalously strong easterlies that JET2000 detected at that latitude between 900 and 800 mb. Note that Fig. 2 is based on data with lower horizontal and vertical resolution than the JET2000 measurements, which were also not instantaneous, but were staggered over an interval of about 8 h.

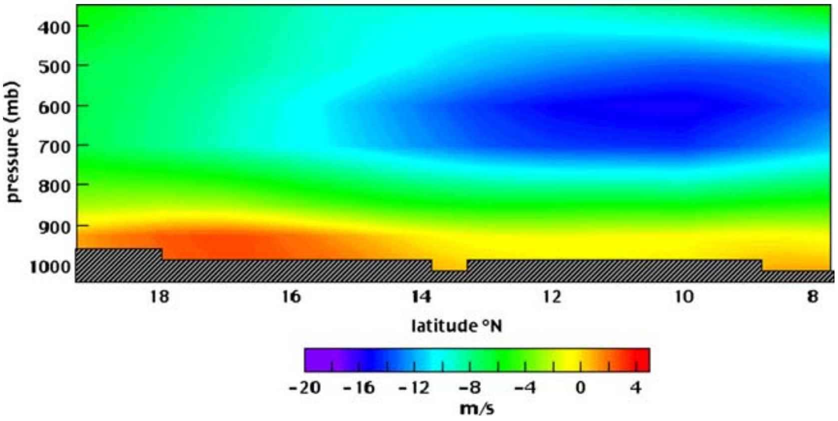

Fig. 2 Latitude–pressure cross-section of the RM3 zonal wind speed along 2.5°E, averaged between 06 UT and 12 UT on 29 August 2000

The meridional temperature gradient over West Africa is strengthened during early summer as the cool Atlantic monsoon air mass moves northward, displacing hot Saharan air. This temperature gradient, which is enhanced by latent heat release within the convective towers of the ITCZ (Thorncroft and Blackburn 1999), creates a westward-directed vertical wind shear (thermal wind) that causes the near-surface monsoon westerlies to reverse direction with altitude, ultimately creating the AEJ. Vertical wind shear associated with the AEJ is also a source of energy from which AWD can grow, in this case through baroclinic instabilities. Figure 3a shows the JJAS 1998–2003 RM3 ground surface temperatures over West Africa, and Fig. 3b shows the corresponding NCPR ground surface (skin) temperature distribution. The RM3 Saharan temperature maximum is some 2°K lower, while RM3 Gulf of Guinea coastal temperatures are 1–2°C warmer than NCPR, causing a weaker RM3 northward temperature gradient. RM3 surface air temperatures (Fig. 3c) are quite close to CRU JJAS 1998–2000 values (not available after 2000) over the Gulf of Guinea coastal region (Fig. 3d), but they are 3–5°K lower than CRU over the Sahara, reinforcing the assessment that the regional model's ground temperatures are too low there. Druyan et al. (2004) point out that a weak meridional gradient of ground surface temperature over West Africa could in turn weaken the negative zonal wind shear, and consequently the AEJ core speed, although Fig. 1 shows that this was not the case in these model results.

Figure 4 compares the horizontal distribution of RM3 JJAS precipitation rates averaged over all six seasons (Fig. 4a) to the corresponding analysis of TRMM estimates (Fig. 4b). Figure 4c shows RM3 minus TRMM differences based on an interpolation of TRMM values to the 0.5° grid. The two representations

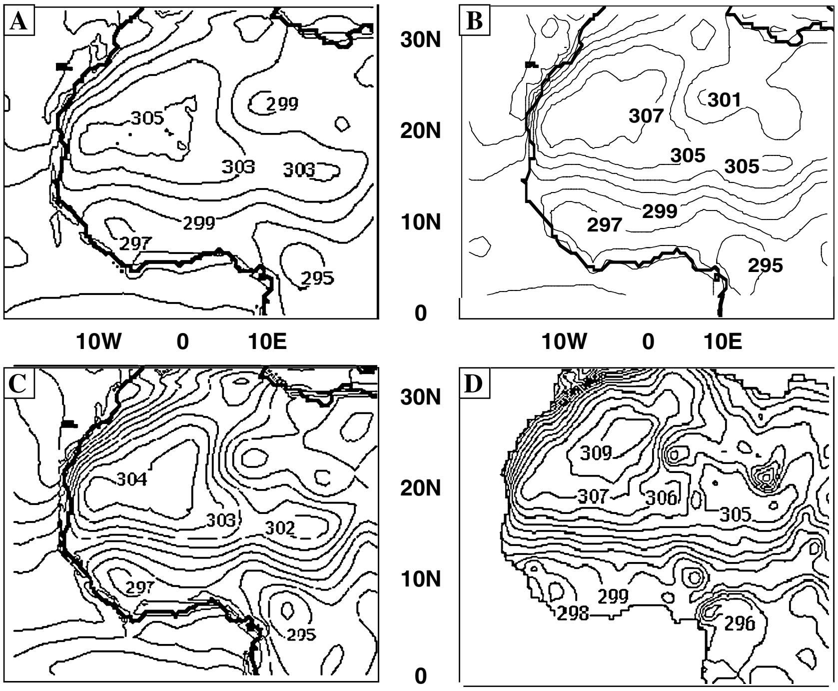

Fig. 3 **a** RM3 mean JJAS 1998–2003 ground temperatures, **b** NCEP reanalysis mean JJAS 1998–2003 "skin" temperatures (Courtesy of CDC/NOAA), **c** RM3 mean JJAS 1998–2000 surface air temperatures and **d** CRU mean JJAS 1998–2000 surface air temperatures (Courtesy of East Anglia University)

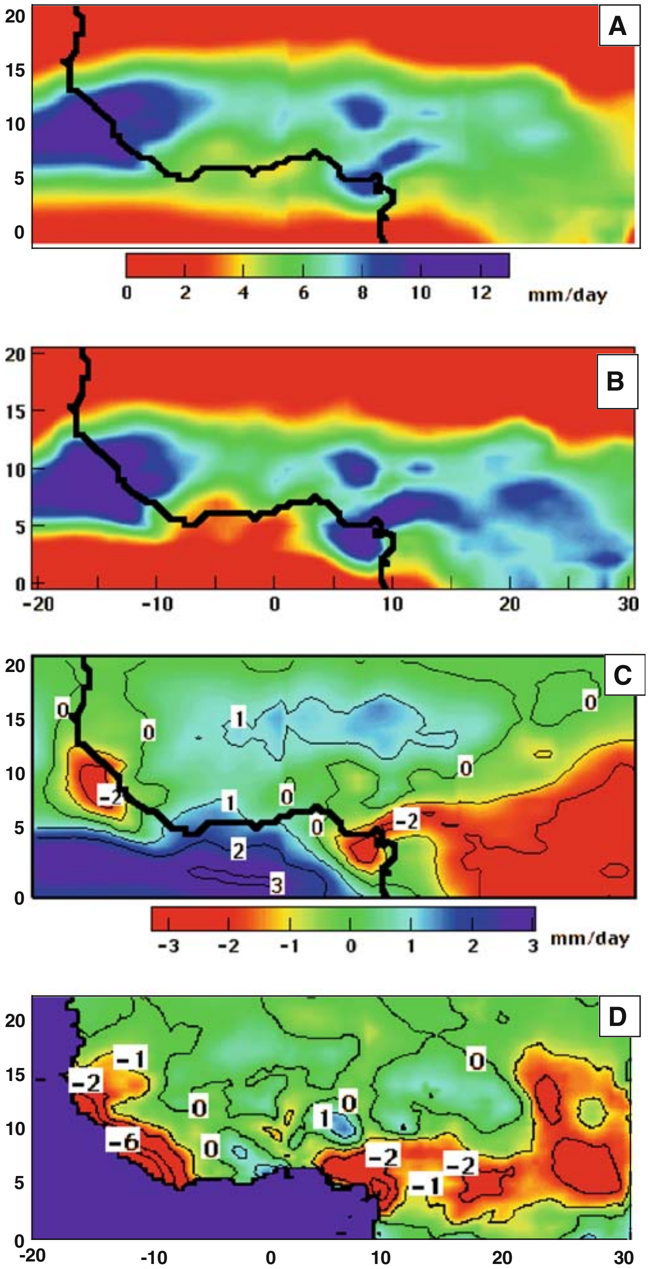

Fig. 4 JJAS mean precipitation rates and differences (mm day^{-1}), **a** RM3, 1998–2003, **b** TRMM, 1998–2003 (Courtesy of Distributed Active Archive Center, NASA/Goddard Space Flight Center), **c** RM3 minus TRMM, 1998–2003, **d** RM3 minus CRU (Courtesy of East Anglia University) for 1998–2000

indicate similar rainfall maxima near 10°N over parts of West Africa, parallel and slightly south of the AEJ core of maximum easterlies (Fig. 1a). Both distributions also indicate orographic maxima, over the southwest coast and at the Camaroon "corner" near 8°E, but RM3 amounts are slightly lower. The RM3 Intertropical Convergence (ITC) maximum is meridionally wider than the TRMM pattern between 0 and 10°W, a consequence of more frequent simulation of moderate rainfall along the northern and southern edges than is perhaps realistic. Thus, RM3 rates exceed TRMM along 15°N and over the Gulf of Guinea. Both the RM3 and TRMM data show the sharp transition over the Sahel between the rainy zone and the dry Sahara.

The CRU (New et al. 2002) monthly mean precipitation rates, interpolated to a 0.5° grid over land, are available for the 1998–2000 seasons. Since these data are often interpolated over substantial distances between reporting stations, they should not be considered an absolute standard for validation. Figure 4d shows the RM3 minus CRU precipitation differences for JJAS 1998–2000. The RM3 validates slightly better against these data over much of the rain belt, although very high CRU rates along the immediate southwest coast are not matched by the RM3 (or TRMM). RM3 rates are some 2 mm day^{-1} too low against both standards along 5°N east of 10°E.

Figure 5a, b compares respectively the RM3 and TRMM time–latitude evolution of daily West Africa rainfall rates averaged between 15°W and 10°E over the 6 years. For this comparison, TRMM data were interpolated to the 0.5° grid. Both representations clearly show the northward jump of maximum rainfall from 5 to 11°N in late June, a recurring intraseasonal transition documented with station data by Sultan and Janicot (2000). In addition to the mid-summer precipitation maximum along 11°N, both analyses show the gradual southward retreat of the ITC during September. RM3 consistently produces a wider swath of rates between 2 and 5 mm day^{-1} along the southern edge throughout the summer, but maximum values are similar for the two representations. Both analyses also show the breaks in heavy rainfall evident in the 6-year means on July 12 and July 26.

4.2 Validation of precipitation variability

The bar graphs in Fig. 6 represent the frequency of binned precipitation intervals in the two data sets for Fig. 5a, b (including TRMM interpolated values), which refer to the area bounded by 0–20°N, spatial averages over 15°W–10°E and 1998–2003 time averages. The biggest difference between the frequency distributions is that TRMM has about 60% more values between 0 and 2 mm day^{-1} than RM3, while RM3 precipitation rates favor mid-range values. The frequency of RM3 precipitation rates in each of the four bins between 2 and 10 mm day^{-1} exceeds corresponding TRMM frequencies, although both distributions indicate a large decrease for rates greater than 8 mm day^{-1}.

Xue and Shukla (1993) showed precipitation "footprints" of AWD in time–longitude cross-sections from simulations with a GCM at an equivalent horizontal resolution of 1.8° by 2.8° (~200×300 km). The diagonal swaths of precipitation maxima and divergence extremes in Fig. 7 show the time–longitude variability for an entire JJAS season, while Figs. 8 and 9 provide a closer look at one segment of the record. Many diagonal

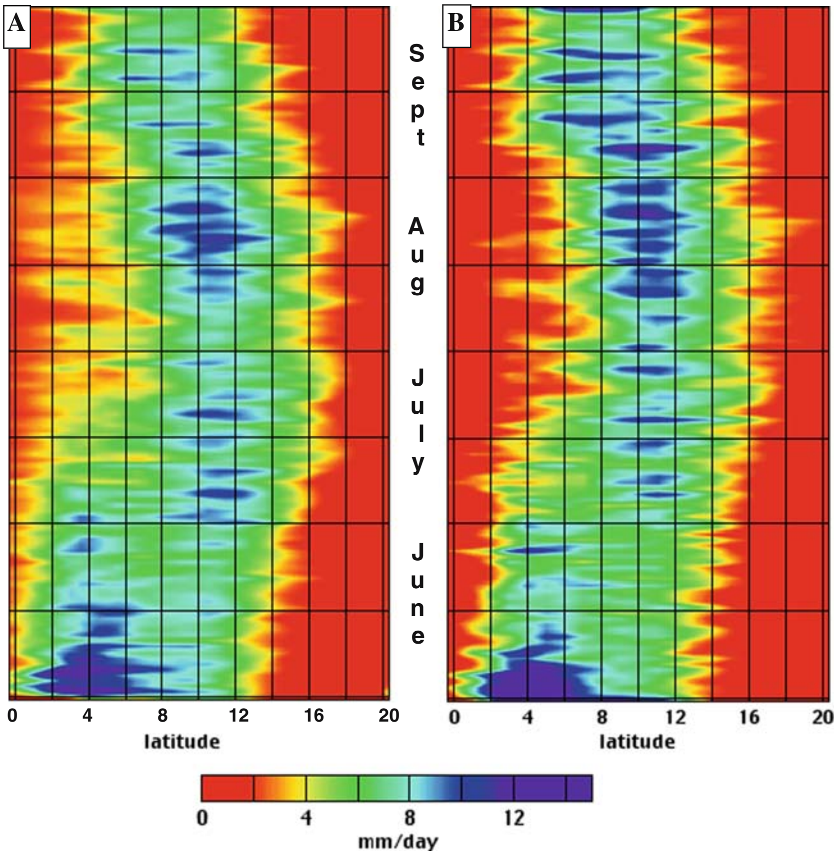

Fig. 5 Time–latitude distributions of daily precipitation rates (mm day^{-1}) averaged over 15°W–10°E for 1998–2003, **a** RM3, **b** TRMM (Courtesy of DAAC/GSFC)

swaths are presumably associated with westward propagating AWD. The first two Hovmöller time–longitude diagrams show respectively, daily precipitation rates for TRMM JJAS 1998 estimates (Fig. 7a) and for the RM3 JJAS 1998 simulation (Fig. 7b), averaged over 5–15°N. Note the close correspondence between RM3 and TRMM precipitation swaths, corroborated by a correlation coefficient of 0.90 between the data sets. Thus, these two representations from two independent systems depict nearly the same space-time distribution of precipitation over West Africa during JJAS 1998, and each validates the other. In this example, however, TRMM maximum rates are consistently greater than corresponding RM3 amounts, although model episodes of no rain are much less frequent than for TRMM.

Similarly congruent TRMM versus RM3 time–longitude diagonal patterns were obtained for each of the other five seasons. Table 1 shows the statistics for comparisons between the RM3 and TRMM daily precipitation rates used to construct time–longitude Hovmöller diagrams for each JJAS season (not shown), as in the example shown in Fig. 7a, b for JJAS 1998. Recall that precipitation rates were averaged over 5–15°N for each longitude. Since each data array is composed of 91 longitudes between 20°W and 25°E for each of 122 days, each statistic is based on the comparison of 11,102 values. The high correlations, averaging 0.88, reflect the congruence of the time–longitude distributions of precipitation rates from the two independent systems. The RM3 mean precipitation rates in all but one case are within 1 mm day^{-1} of the corresponding TRMM means. The average RM3 minus TRMM difference for the six seasons is close to zero, but RM3 daily precipitation rates have considerably lower variance.

Summer monsoon rainfall over West Africa occurs within zones of predominantly near-surface convergence and upper tropospheric divergence (Druyan 1998). However, transient disturbances modulate the mean divergence regime. More of the time–space distribution of the segment of 925 mb divergence shown in Fig. 7c has negative rather than positive values, but there are several bands of strong convergence that propagate westward, and some of these coincide with precipitation bands. Some incongruence between precipitation and 925 mb convergence can perhaps be explained by the comparison of 24 h accumulations with a derivative of instantaneous (12 UT) simulated winds. Positive divergence is more prominent on the time–space distribution shown in Fig. 7b for 200 mb. This pattern includes only a few segments of what might be westward moving divergence centers during this period. Druyan (1998) found in a GCM study that precipitation associated with simulated AWD was enhanced when the system moved under centers of 200 mb divergence, but that the latter rarely moved in tandem with the disturbances. The same study also found that 200 mb divergence patterns over West Africa in the simulations were dominated by weekly time scales, changing more slowly than their

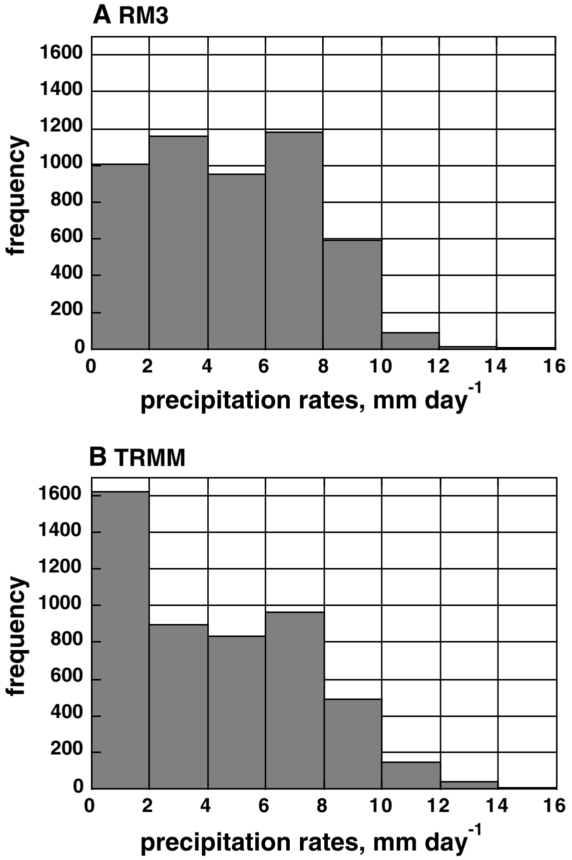

Fig. 6 Frequency distributions of the values plotted in Fig. 5: **a** RM3, **b** TRMM (Courtesy of DAAC/GSFC)

lower tropospheric counterparts. In Fig. 7d, 200 mb divergence, conducive to the positive vertical motion that supports precipitation, becomes more frequently positive by July and remains so through September. In contrast to the more regular pattern at 925 mb, divergence at 200 mb is not generally organized along diagonal bands. In fact, many of the 200 mb divergence maxima span a wide range of longitudes and many correspond to precipitation episodes.

The Hovmöller diagrams in Figs. 8 and 9 show the details of several precipitation-related systems between July 31 and August 23, 1998. TRMM observations (Fig. 8a) show some nine diagonal precipitation bands, and all of them are simulated by the RM3 (Fig. 8b), albeit with lower rates. NCPR (Fig. 8c), on the other hand, did not simulate distinct precipitation bands at all, even missing some of the more prominent events altogether, such as on August 17–22, 10–20°E. In fact, the time–space patterns of NCPR precipitation are quite different from both the RM3 results and TRMM. The center lines of the RM3 precipitation bands have been superimposed on corresponding Hovmöller diagrams of divergence at 925 mb (Fig. 9a) and 200 mb (Fig. 9b). Many of the precipitation trajectories can be associated with westward propagating centers of strong convergence at 925 mb, and parts of some of the segments pass under episodes of strong 200 mb divergence. Some of the westward propagating 925 mb convergence bands merge with a quasi-stationary center of convergence along 12–16°W. The precipitation maximum that moves from 5°E to 20°W during August 12–16 follows one such 925 mb transient convergence band below strong 200 mb divergence. On the other hand, the rather well organized precipitation segment between 23°E and 3°W during August 5–8 does not correspond to any parallel divergence patterns at either level. This may have been a squall line associated more with local heating than with a propagating convergence area detectable by the 0.5° horizontal grid spacing. The diagonal slopes of the TRMM and RM3 precipitation bands (Fig. 8a, b) imply westward movement, although the spatial distribution of precipitation is not an ideal marker for computing wave speed. The propagation speeds, implied by the examples on Fig. 8b, average about 7.4° day^{-1} (8.6 ms^{-1}), quite representative of AWD (Reed et al. 1977).

Figure 8a, b indicates that by August 2–3 rather heavy precipitation (averaged between 5 and 15°N) was moving in from the east to longitudes 13–18°W, with lower rates lingering near 12°W. Thus, the heaviest rainfall occurs downstream of the 700 mb trough (see the rainfall distribution for August 2, discussed below) and within near-surface converging westerly and southwesterly circulation south of the low-level cyclone. Figure 9a, b indicates that the strong near-surface convergence that arrived from the east with the rain had strong upper-tropospheric divergence west of 15°W, which undoubtedly enhanced the moist convection.

Both TRMM data and RM3 precipitation simulations show interannual variability over the domain of interest. Precipitation anomalies were formed by subtracting 6-year means from each seasonal precipitation distribution (Fig. 10). Similarly, precipitation anomalies are also shown for only August of each year (Fig. 11), climatologically the height of the rainy season. Figures 10 and 11 show that the RM3 JJAS 2002 simulation was rainier than the other seasons. Corresponding positive, albeit somewhat smaller, anomalies are evident in the TRMM data for August 2002 over the Atlantic ITCZ (7°N) and near 8°E. Indeed, many of the larger TRMM anomalies during the other seasons are also qualitatively reproduced by the RM3. For example, TRMM data for JJAS 1999 indicate a dipole pattern of heavy precipitation along 4°N and somewhat drier conditions over parts of West Africa along 10°N, a pattern that is nicely captured by the RM3. Similarly for JJAS 2000, JJAS 2001 and JJAS 2003, negative precipitation anomalies over the Gulf of Guinea and the Atlantic near 5°N overlap in both analyses. TRMM and RM3 August precipitation anomaly patterns (Fig. 11) have many features in common.

Thorncroft et al. (2003) published a time series of the mean rainfall for July–September 2000 within the area bounded by 13–13.9°N, 1.7–3.1°E (which is near Niamey), based on 34 rain gauges. As an independent check on modeled precipitation rates, Fig. 12 compares these

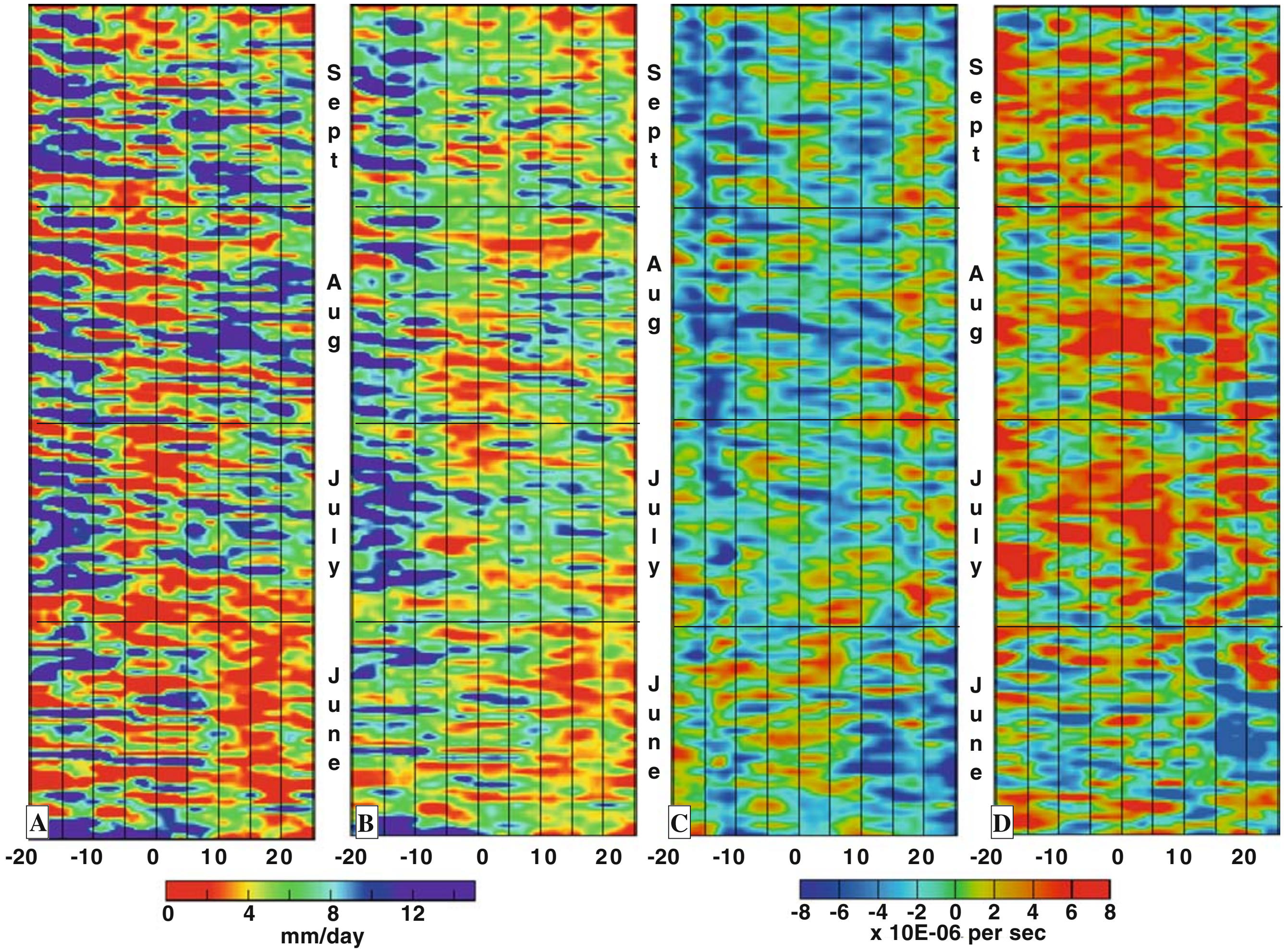

Fig. 7 Time–longitude distributions for JJAS 1998 of **a** TRMM (Courtesy of DAAC/GSFC) daily precipitation rates averaged over 5–15°N, **b** RM3 daily precipitation rates averaged over 5–15°N, **c** RM3 925 mb divergence averaged over 8–12°N and **d** RM3 200 mb divergence averaged over 8–12°N. Precipitation units: mm day^{-1}. Divergence units: $\times 10^{-6}$ s^{-1}

Table 1 Statistics of comparisons between RM3 and TRMM daily precipitation rates averaged over 5–15°N for 20°W–25°E (as in Fig. 7a, b)

Year	RM3 mean (mm day^{-1})	TRMM mean (mm day^{-1})	RM3 variance (mm^2 day^{-2})	TRMM variance (mm^2 day^{-2})	RM3 minus TRMM mean (mm day^{-1})	RM3 vs. TRMM correlation coefficient
1998	6.0	6.6	11.1	30.0	−0.5	0.90
1999	5.7	6.6	10.8	24.0	−0.9	0.90
2000	6.1	6.4	11.0	24.6	−0.4	0.86
2001	6.3	6.1	10.2	23.1	0.2	0.83
2002	8.2	6.2	18.7	24.8	2.1	0.90
2003	6.3	7.0	10.1	24.4	−0.6	0.88
1998–2003	6.4	6.5	12.0	25.1	−0.02	0.88

The last row shows 1998–2003 means for each statistic

data with RM3 results from 15 co-located model grid elements of the JJAS 2000 simulation (and with co-located TRMM daily estimates). Although the model underestimated many of highest daily amounts and produced light rain on many days that were actually dry, the RM3 captured the timing of all observed major precipitation events. TRMM daily estimates also validate quite well against the rain gauge data, except for lower extreme values on several very rainy days. Table 2 gives the correlation coefficients between the time series shown in Fig. 12. Results for the two systems that provide spatially integrated precipitation (RM3 and TRMM) are more highly correlated with each other than with the discreet point information observed by the

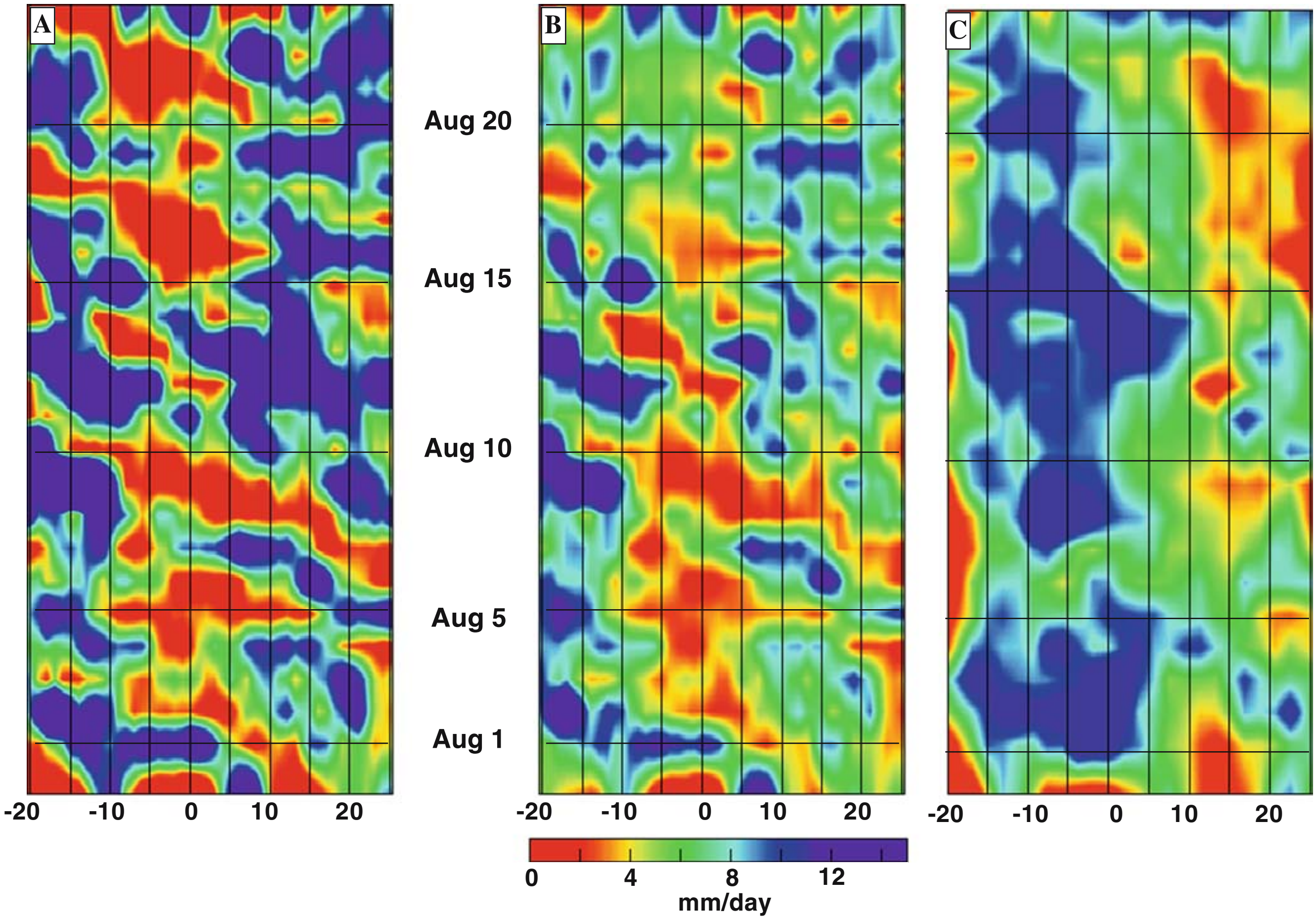

Fig. 8 Time–longitude distributions between July 31 and August 23, 1998: **a** TRMM daily precipitation rates (mm day^{-1}) (Courtesy of DAAC/GSFC), averaged over 5–15°N, **b** RM3 daily precipitation rates (mm day^{-1}), averaged over 5–15°N, **c** NCPR daily precipitation rates (mm day^{-1}) (Courtesy of CDC/NOAA), averaged over 5–15°N

rain gauges. The favorable comparison is consistent with the more extensive validation of RM3 precipitation against TRMM data that is discussed above.

4.3 Investigation of periodic fluctuations

A zone of maximum vorticity variance is created along a trajectory of transient cyclonic disturbances. Accordingly, Reed et al. (1988) deduced AWD trajectories in gridded data from the ECMWF analysis and forecast archive projected on a 3° by 3° latitude–longitude grid by mapping the 700 mb vorticity variance filtered for 2.9 to 4.0 and 2.9 to 4.7-day periods. Their analysis was confined to August–September 1985 and their Fig. 4 showed a northerly AWD track along 21°N as well as a more southerly one between 12 and 15°N. Subsequently, Thorncroft and Hodges (2001) tracked AWD vorticity maxima at 600 and 850 mb over West Africa and the Atlantic Ocean during the 20-year period 1979–1998. They used ECMWF analyses created by assimilating observations at a similar horizontal resolution (T42 or about 2.8°), showing the most frequent trajectories crossing West Africa along approximately 10°N. Figure 13 shows spatial distributions of variances of 700 mb vorticity time series (four times per day) from August 1 to September 30, filtered for 3 to 6-day periods from each season simulated by the RM3. Note the considerable interannual variability in the patterns, manifest in a range of amplitudes and different implied AWD trajectories. The higher resolution of the RM3 compared with ECMWF used in the previous studies allows the determination of the AWD trajectories with greater spatial precision. Moreover, vorticity variances are also stronger than those based on the lower resolution ECMWF analyses. The distribution for August–September (AS) 1998 (Fig. 13a) indicates one AWD trajectory along 21°N, and a second near 13°N, similar to the Reed et al. (1988) results for 1985. In fact, the patterns for five of the 6 years (except AS 2000) also imply dual tracks. During AS 1999, the southernmost maxima imply a diagonal AWD path crossing from 6 to 13°N (Fig. 13b), similar to the Thorncroft and Hodges (2001) mapping based on vorticity maxima. The AS 2000 and AS 2002 data imply very distinct tracks closely following 11°N (Fig. 13c) and 15°N (Fig. 13e), respec-

Fig. 9 Divergence of the RM3 circulation at 12 UT each day, 31 July–23 August, 1998, averaged over 8–12°N. **a** 925 mb, **b** 200 mb. The trajectories of RM3 westward propagating precipitation maxima (from Fig. 8b) are superimposed. Divergence units: $\times 10^{-6}\ \mathrm{s}^{-1}$

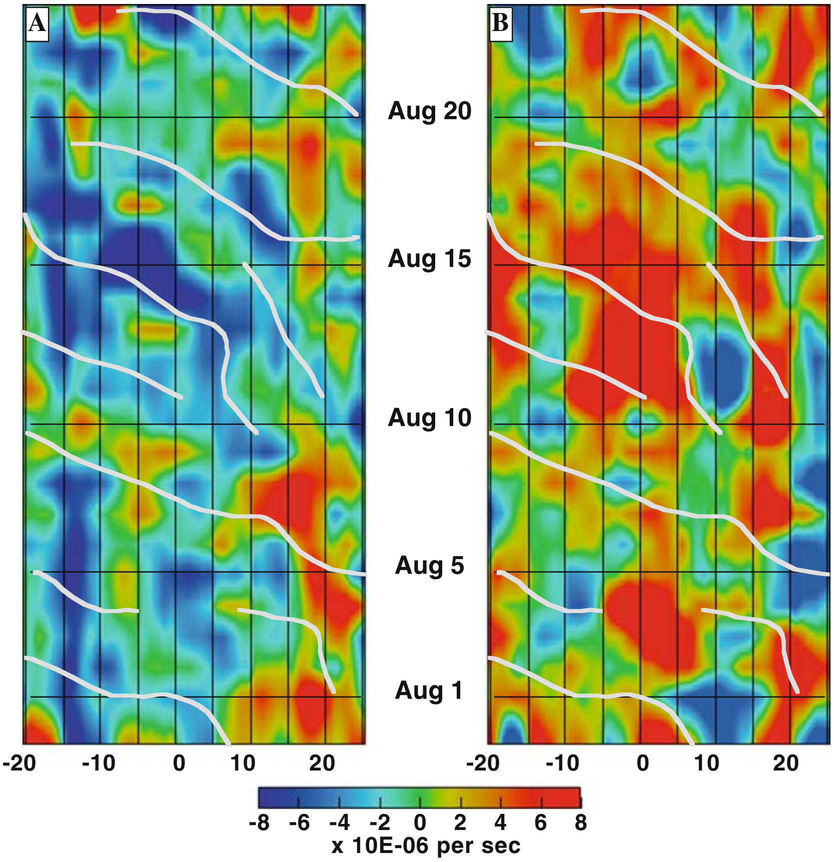

tively. Vorticity variance amplitudes are particularly strong for AS 2001 (Fig. 13d) over Atlantic coastal waters.

Observations show that AWD often feature closed cyclonic circulations in the lowest atmospheric layers, which are associated with open wave structures near 700 mb. AWD that traverse West Africa cause periodic wind fluctuations, most prominently in the meridional component of the circulation. Amplitudes of these fluctuations are strongest in the mid-troposphere, usually at about 700 mb, south of the AEJ, although according to Pytharoulis and Thorncroft (1999), at lower altitudes farther north.

Once daily (at 12 UT) 700 mb meridional wind components (*v7*) for RM3 versus NCPR and ERA-40 August 2002 analyses are compared. Figure 14 shows the three respective Hovmöller time–longitude plots of *v7*, averaged over 5–15°N. The patterns for all three analyses describe westward propagating centers of alternating southerly and northerly circulation, and the timing for each data set is closely synchronized with the others. The slopes of the alternating positive and negative bands imply AWD westward speeds of 5°–10° per day (5.8–11.6 ms^{-1}), and longitudinal distances between adjacent maxima or minima imply wavelengths of about 35° (approximately 3,500 km) and approximately 5-day periods. Reed et al. (1988) deduced 2,500 km AWD wavelengths from ECMWF data gridded with 3° spacing, but the finer RM3 computational grid allows more precise estimates. These speeds, periods and wavelengths are representative of estimates from previous empirical studies (Burpee 1972; Reed et al. 1977; Druyan et al. 1996). Despite the great similarities in the timing of *v7* extremes, NCPR and ERA-40 *v7* clearly range between more extreme positive and negative values than the corresponding RM3 *v7*, so NCPR and ERA-40 AWDs have considerably higher amplitudes than RM3 AWDs. Moreover, model dependence is reflected in the occasional discrepancies in the locations of *v7* extremes between the NCRP and ERA-40 representations, even though both are partially based on observations. Comparisons for the other years were consistent with this evaluation, as can also be seen in Fig. 15. Figure 15 compares 12 UT values of the 5–15°N averaged *v7* along 7.5°W during each day in August for the RM3 and for the corresponding NCPR and ERA-40 (1999–2002). The RM3 time series of *v7* are highly correlated with the NCPR *v7* time series ($0.86 \le r \le 0.97$), but the frequently lower amplitude of most RM3 *v7* oscillations is evident. Figure 15 also shows that the ERA-40 agrees with NCPR regarding the timing of the most prominent v7 oscillations ($0.82 \le r \le 0.92$), although the data imply that ERA-40 AWD amplitudes are often lower than NCPR. As an independent check on the realism of the RM3 circulation, we note that the five RM3 time series are also highly correlated with these ERA-40 data ($0.76 \le r \le 0.86$), the poorest correlation occurring for August 2000, which experienced the lowest variability of *v7*.

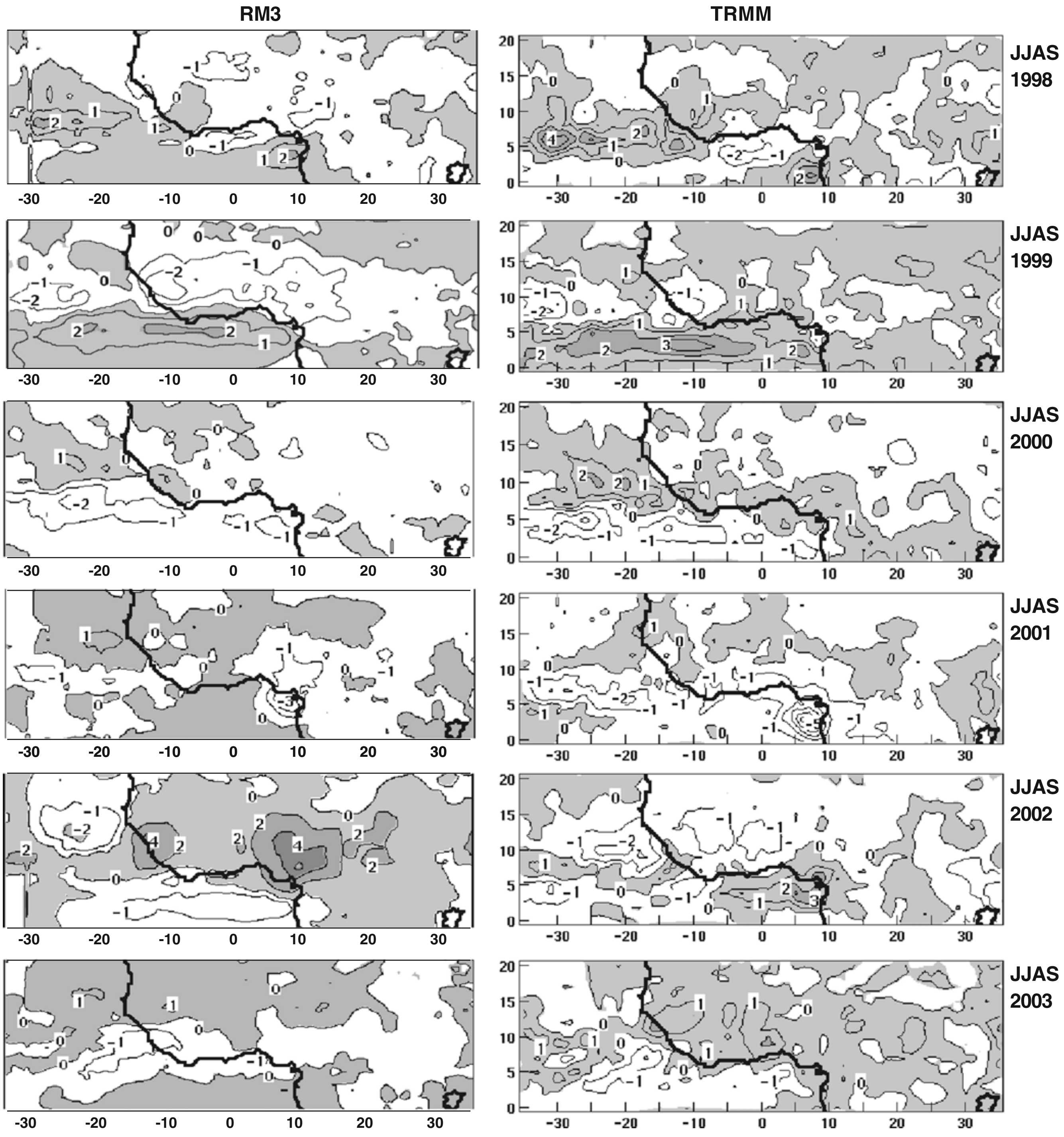

Fig. 10 JJAS precipitation anomalies (mm day^{-1}) for each summer relative to 1998–2003 means. *Left* RM3, *right* TRMM

Periodic fluctuations of *v7* can be monitored by fast Fourier transform (FFT) spectral analyses of time series. AWD are detected as FFT spectral peaks, most often at periods within the 3–6 day range (Burpee 1972; Reed et al. 1977; Druyan et al. 1996). Diedhiou et al. (1999) have also discussed the occurrence of 6–9 day periodic circulations over West Africa. FFT spectra were prepared from RM3 four times daily *v7* time series at each grid element and the ASA was computed for peaks occurring between 3 and 6-day periods. Before discussing the spatial distributions of these ASA, sample FFT spectra are examined (Fig. 16) at a representative grid element, 15°N, 12°W. In order to discern how spectral peaks stand out above red noise, the FFT *v7* spectra are shown as departures (most of which are statistically significant at the 95% confidence interval) from fitted

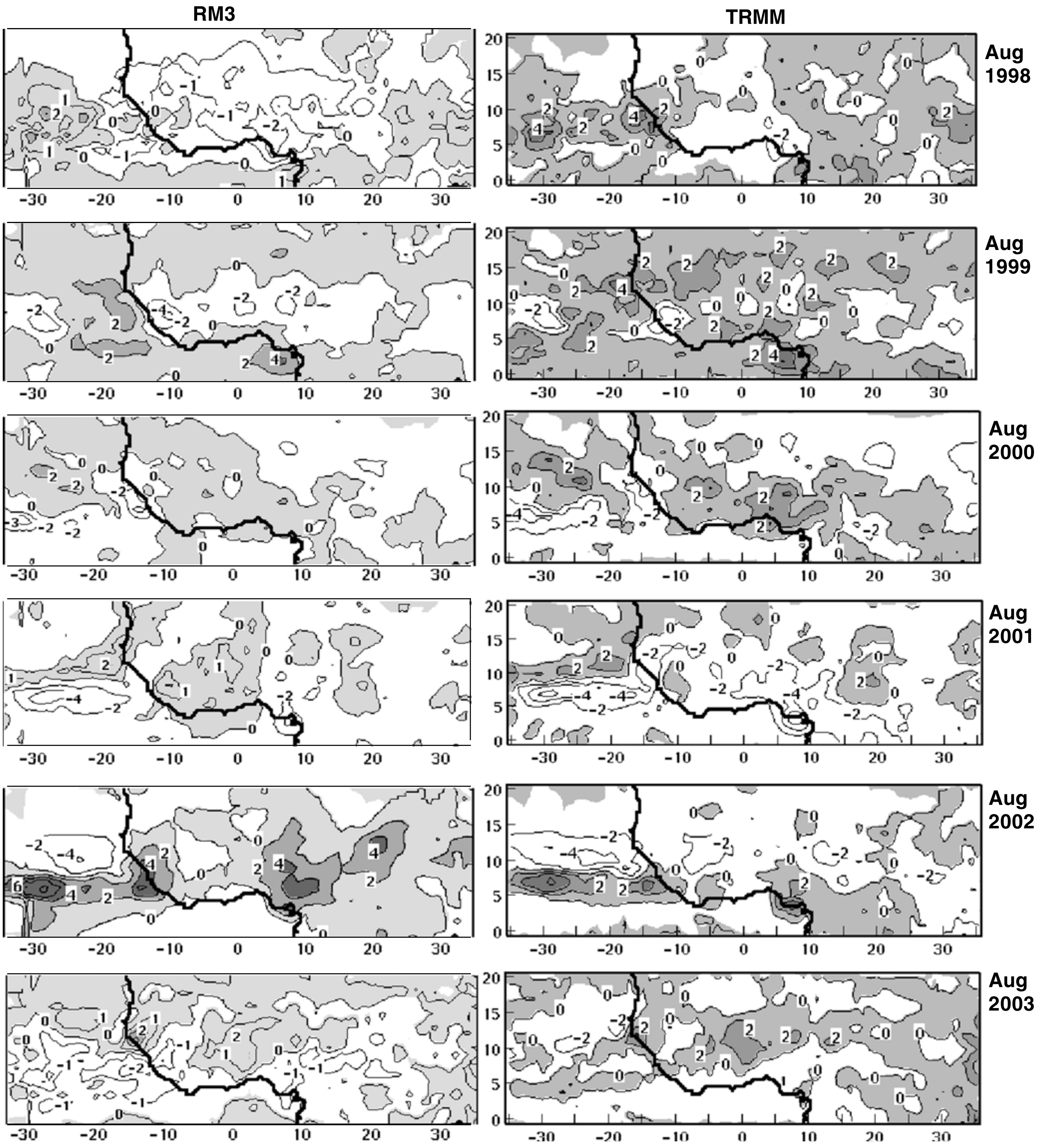

Fig. 11 August precipitation anomalies (mm day^{-1}) for each year relative to 1998–2003 means. *Left* RM3, *right* TRMM

power curves. Figure 16a shows the average of the six JJAS seasonal spectra, and Fig. 16b shows the single FFT spectrum for JJAS 2002. The greatest spectral amplitudes in Fig. 16a, which stand out above red noise, indicate a predominance of periodic activity between 3.5 and 5.3 days, typical of AWD. Amplitudes have been somewhat dampened in creating the 6-year mean since sharp peaks often occur at slightly different periods each year. Figure 16b shows that the spectral peak for JJAS 2002, at 5 days, is about 50% higher than the 6-year mean peak, while a secondary peak is evident at 4 days. Figure 16c shows the spectrum of daily precipitation for JJAS 2002 within the zone immediately south of 15°N, 12°W. Its highest peak, statistically significant at the

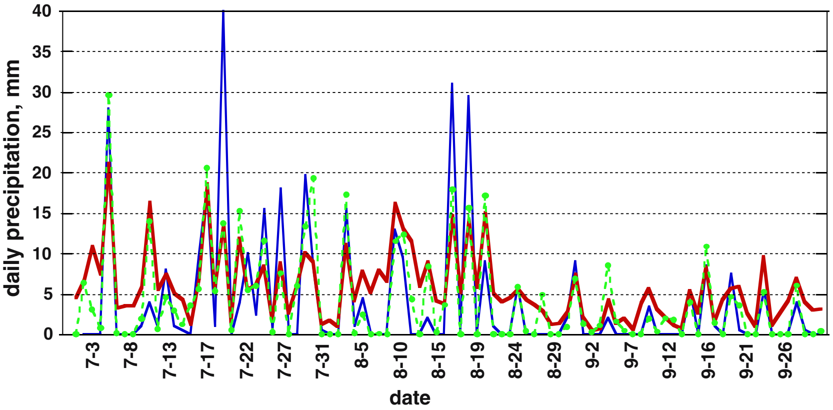

Fig. 12 Time series of the mean of 34 daily rain gauge observations (*blue*) within the area bounded by 13–13.9°N, 1.7–3.1°E (Thorncroft et al. 2003) versus RM3 daily values (*red*) for 15 co-located grid elements and TRMM daily estimates (*green*) for four co-located 1° squares, July–September 2000

Table 2 Correlation coefficients between time series of daily rainfall during July–September 2000

	RM3	TRMM
RG	0.73	0.79
RM3		0.86

RG (from Thorncroft et al. 2003): average of 34 rain gauge measurements within the area bounded by 13–13.9°N, 1.7–3.1°E. *RM3*: average of model precipitation at 15 grid elements, 13–14°N, 1.5–3.5°E. *TRMM* (Courtesy of Distributed Active Archive Center, NASA/Goddard Space Flight Center): average of daily estimates at four squares, 13–14°N, 2–3°E

95% confidence level, also indicates a strong 5-day periodicity for precipitation events, matching the *v7* spectrum. Several peaks for shorter periods imply other mechanisms of rainfall variability, although the daily sampling does not provide resolution below 2-day periods. Figure 16d shows the season versus period cross-section of FFT spectral amplitudes for *v7* JJAS time series at 15°N, 12°W. Most of the high amplitudes are concentrated in the 3 to 6-day period interval, but there is considerable interannual variability of spectral peaks.

Intraseasonal variability of the spectral signature of *v7* can be diagnosed using wavelet analysis (Taleb and Druyan 2003; Torrence and Compo 1998). Taleb and Druyan (2003) assumed that AWD were affecting the weather at a West African station whenever the wavelet amplitude was large enough to be statistically significant. Figure 17a shows the wavelet analysis at 15°N, 12°W for the four times daily *v7* time series during JJAS 2002. White areas indicate statistical significance. Results show that the summer experiences alternating active and quiet periods, some of which can last for several weeks. For example, no significant AWD activity was detected during the first half of July or during the last week in August. Moreover, just as Fig. 16d showed the interannual variability of leading periodicities, so too the wavelet analysis in Fig. 17a shows that waves of varying periods traverse the location during different parts of the summer. The 4 to 5-day period signals that are so dominant in Fig. 16b (representing the entire summer) occurred during the second half of June and the first half of August, while 3-day periodicity of *v7* was evident during four brief intervals in July, August and September. Relatively high wavelet amplitudes also frequently occur in the range of 6 to 9-day periods, indicating the kind of waves discussed by Diedhiou et al. (1999), but Fig. 17a shows that such activity exceeded the threshold for statistical significance for only about 1 week toward the end of July. The wavelets for the precipitation time series (within the precipitation zone south of 15°N along 12°W) shown in Fig. 17b are not well correlated with the wavelets for *v7* in Fig. 17a, although there is some overlap of significant periodicity in the two records, such as during the first half of August. However, a strong 3-day period precipitation signal detected during the beginning of June occurs before any periodic *v7* variability is detected. Figure 17c shows the time series of daily precipitation rates used to construct the wavelets in Fig. 17b and a smoothed fit showing lower frequency variations of rainfall during JJAS 2002. Series of heavy rain events clearly occurred during lulls in AWD in the beginning of June and July. A few heavy rain events are apparently associated with the AWD activity of early August, but rather heavy precipitation, exhibiting 4 to 6-day periodicity several weeks later, outlasts the significant *v7* wavelets. Taleb and Druyan (2003) and Druyan et al. (1996) emphasized that West African summer precipitation events are sometimes associated with non-wave triggers and, on the other hand, some AWD may lack the moisture for heavy rainfall.

Consider the first few days in August 2002. The *v7* wavelets at 15°N, 12°W indicate 5 to 6-day waves (Fig. 17a) and the daily precipitation time series along 12°W indicates 4 to 5-day variability (Fig. 17b). Figure 18a shows the RM3 700 mb circulation and Fig. 18b the 925 mb circulation, respectively, both at 00 UT on August 3, 2002. The 700 mb wave trough is along 6°W and a closed cyclonic circulation at 925 mb is centered at about 17°N, 12°W, underneath the 700 mb northeasterlies and west of the (700 mb) trough. Note that the center of convergence at 925 mb does not experience heavy rain because of large-scale subsidence and consequently low humidities over the Sahara. The very close correspondence between the spatial distribution of RM3

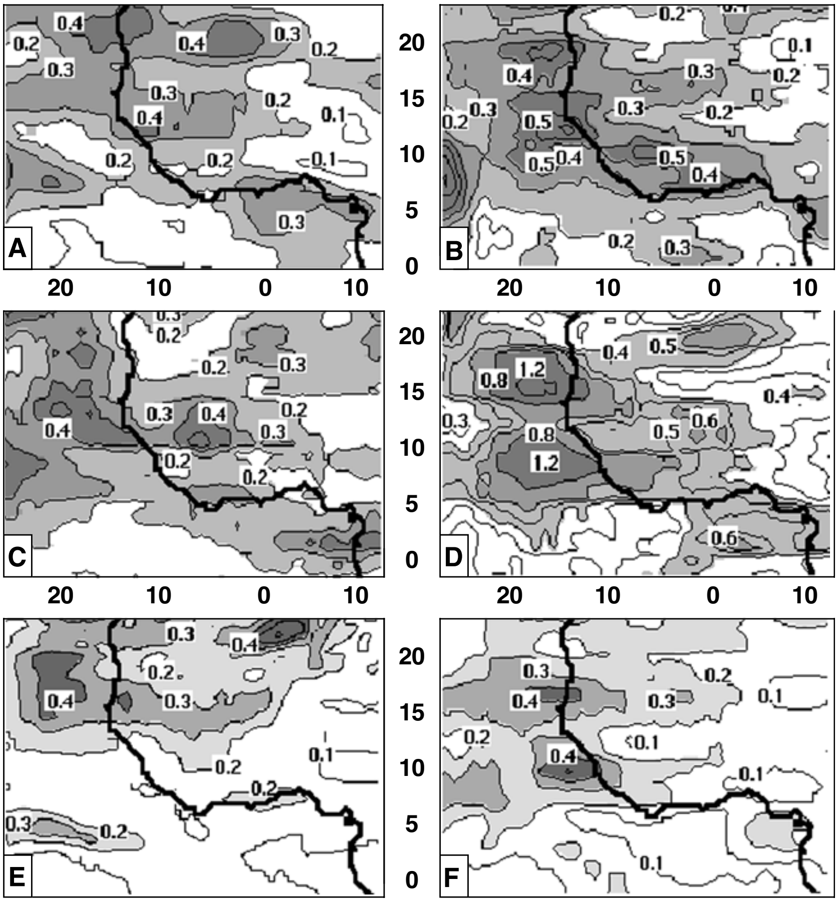

Fig. 13 Spatial distributions of vorticity variance ($\times 10^{-10}\ s^{-2}$) computed from August to September 700 mb vorticity time series filtered for 3 to 6-day periods: **a** 1998, **b** 1999, **c** 2000, **d** 2001, **e** 2002, **f** 2003

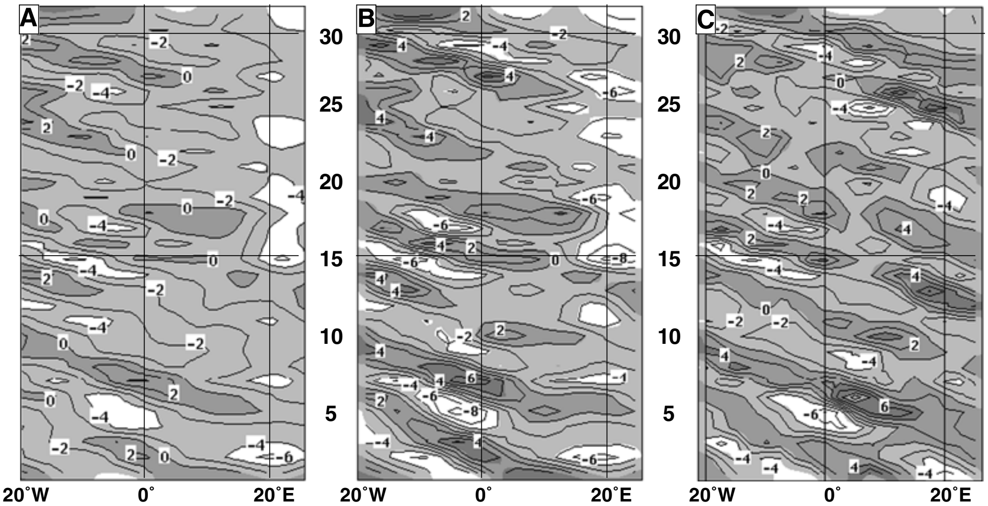

Fig. 14 Time–longitude distributions of the daily 12 UT 700 mb meridional wind component (m s^{-1}) during August 2002, averaged over 5–15°N: **a** RM3, **b** NCPR (Courtesy of CDC/NOAA), **c** ERA–40 (Courtesy of ECMWF)

precipitation (Fig. 18c) versus TRMM estimates (Fig. 18d) suggests that the simulated fields are quite realistic. The Reed et al. (1977) composite AWD based on observations during August–September, 1974 featured a precipitation maximum southwest of the trough apex, as in Fig. 18c, d. Precipitation rates within the northeast section of the large coastal precipitation shield are very likely orographically enhanced, but the offshore portion must reflect mesoscale low-level convergence that may be related to the AWD dynamics. The JJAS 2002 time series of daily *v7* at 15°N, 12°W was compared with the corresponding daily precipitation time series that appears in Fig. 17c, which shows the averages between 5 and 15°N along 12°W. The correlation coefficient of −0.22, significant at about the 97% confidence level, indicates that heavy rain events are favored by

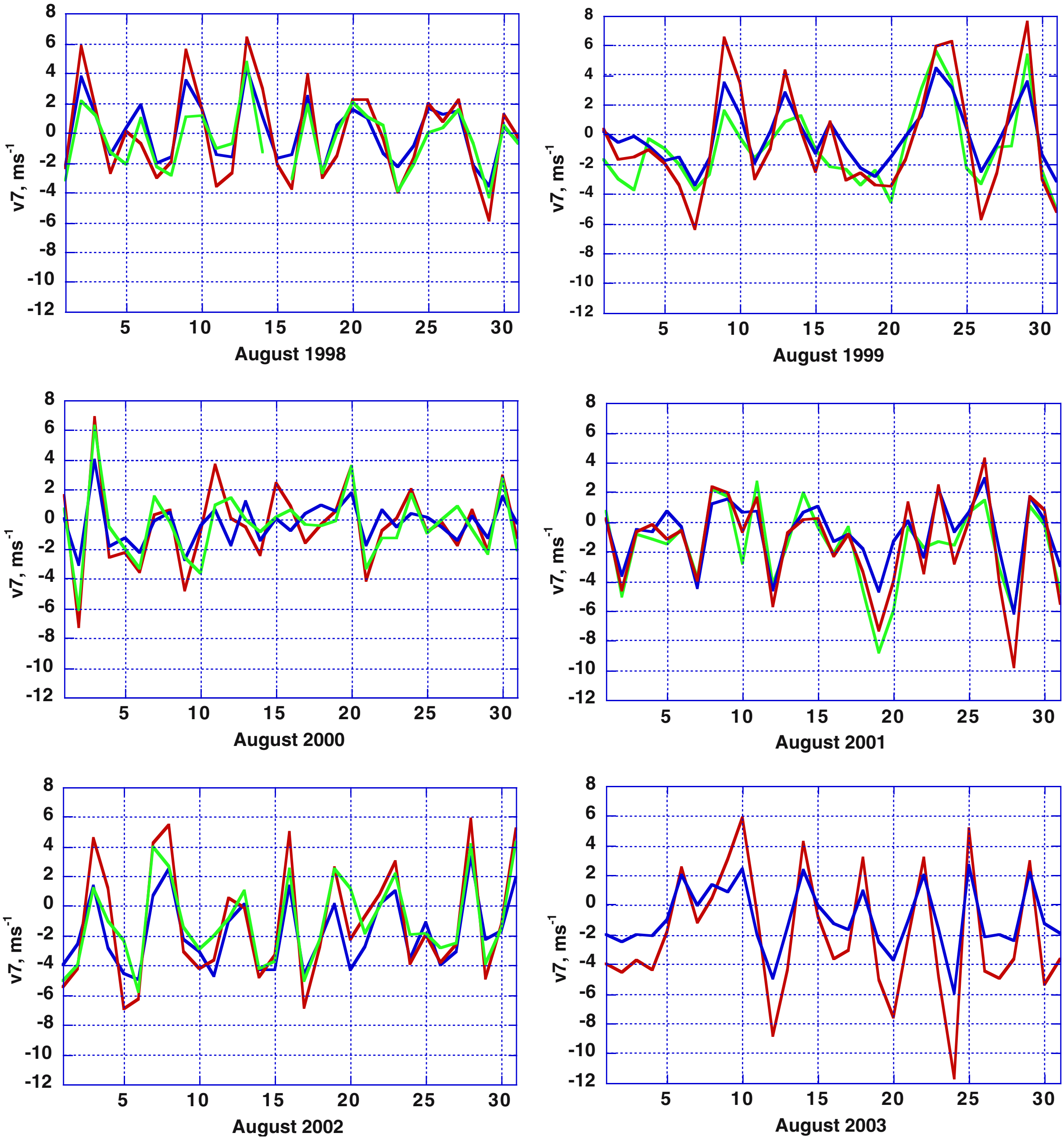

Fig. 15 Comparison of RM3 (*blue*) versus NCPR (*red*) and ERA-40 (*green*) 12 UT 700 mb meridional wind components during each August along 7.5°W, averaged over 5–15°N. (NCPR values courtesy of CDC/NOAA; ERA-40 values courtesy of ECMWF, not available for August 2003)

northerly *v7*, as in the example in Fig. 18. However, this also means that *v7* explains less than 5% of the variance of daily fluctuations of precipitation, so other mechanisms, such as orography and local heating are undoubtedly important too.

Three horizontal distributions of ASA in the 3 to 6-day period interval, constructed for sets of *v7* time series for entire JJAS seasons, are shown in Fig. 19. ASA spatial distributions were also prepared for the second half of each season, from *v7* time series between August 1 and September 30 (but not shown), and they were compared with the spatial patterns of vorticity variance discussed above for Fig. 13. While some of the ASA maxima coincided with vorticity variance maxima, others were displaced some 5° to the south, indicating that these two diagnostics do not always refer to co-located features of AWDs. Duvel's (1990) maps of ASA within the spectral interval 2.8–5.1 days for ECMWF JJ and AS 1983–1985 observational analyses show maxima straddling the Atlantic coast of West Africa near 15°N. The

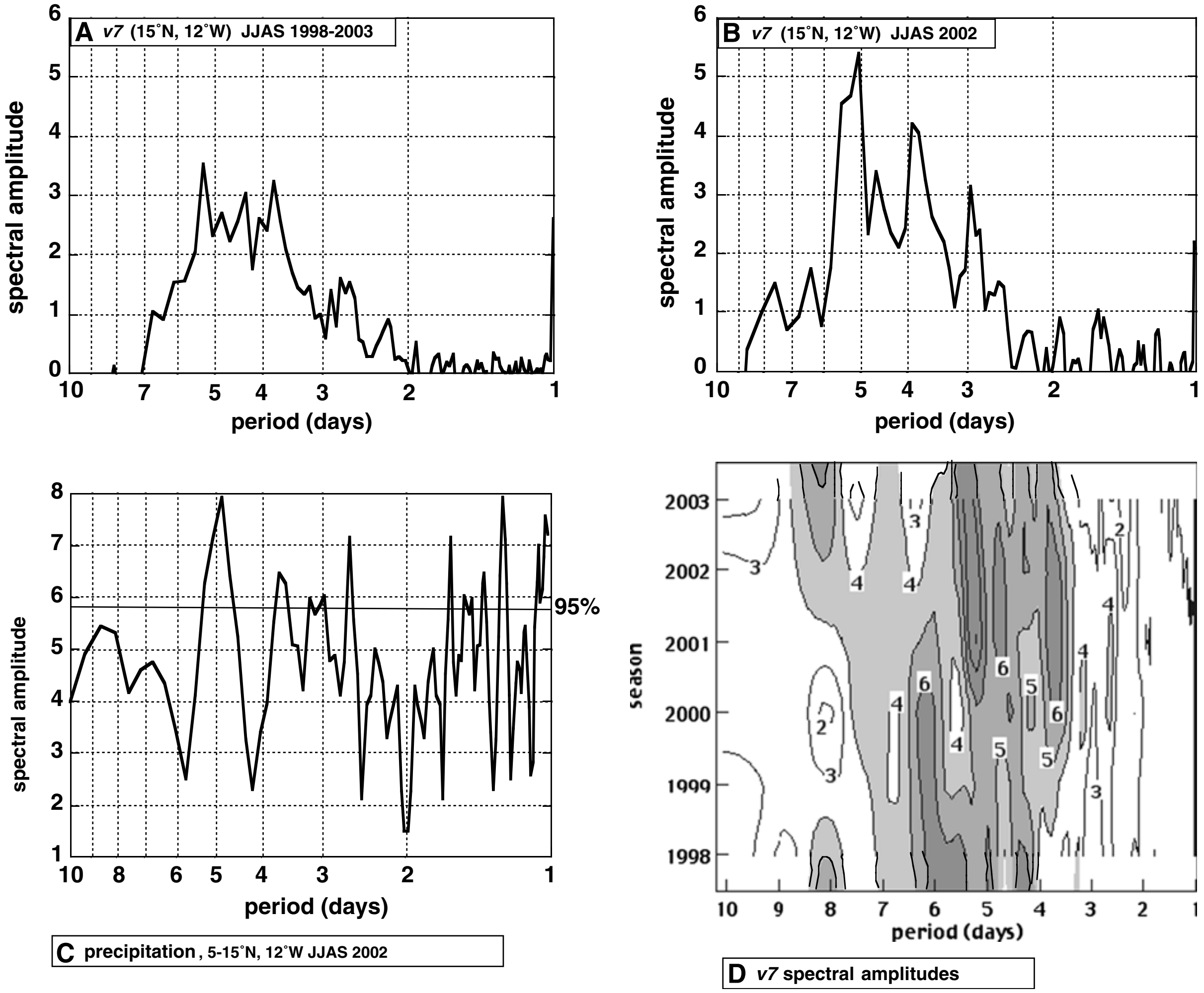

Fig. 16 FFT spectra for JJAS time series of **a** *v7* at 15°N, 12°W, averaged over 1998–2003, **b** *v7* at 15°N, 12°W, year 2002, **c** daily precipitation along 12°W, averaged over 5–15°N, year 2002, **d** *v7* at 15°N, 12°W, season versus period cross-section for 1998–2003. The v7 spectra are shown as departures from fitted power curves representing red noise

RM3 spatial distribution of ASA for JJAS 1998–2003 in the 3 to 6-day period band is shown in Fig. 19a. An eastward bulge in the contours near 17°N indicates higher or more frequent 3 to 6-day period spectral amplitudes than near 10°N. A more pronounced maximum occurs over the Gulf of Guinea along 4°N. The simulated horizontal distributions of ASA show an interesting interannual variability. For example, JJAS 1999 (Fig. 19b) and JJAS 2000 (not shown) have almost no discernable ASA maximum over West Africa, perhaps consistent with the relatively low rainfall over land during JJAS 1999. However, over 4°N the ASA shown in Fig. 19b for JJAS 1999 were some of the highest of all six seasons, coinciding with relatively heavy precipitation there that season. In contrast, the ASA distributions for JJAS 2001, 2002 and 2003 (Fig. 19c) do have maxima near 15°N. Only JJAS 2002 does not have a maximum over the Gulf of Guinea. Interestingly, there is a relative minimum in all years along 10°N, indicating that wave troughs usually assume more northerly trajectories.

4.4 Sensitivity to the resolution of orography

To what extent is the less realistic time–space distribution of NCEP reanalysis precipitation (compared to RM3 results), discussed above in connection with Fig. 8c, a consequence of the coarser resolution orography? The simulation for JJAS 1998 was repeated using the 2.5° grid representation of NCEP reanalysis orography, interpolated to the RM3 grid. This had the effect of smoothing the highest peaks, such as over the Guinea highlands in the southwest and the mountains of Cameroon. Figure 20a shows the errors in the JJAS 1998 mean precipitation rates from this simulation relative to CRU gridded observations (New et al. 2002), and Fig. 20b shows the corresponding errors from the original JJAS 1998 simulation. The low-resolution resolution topography reduced the mean JJAS precipitation rates over most of West Africa, creating broader areas of errors between -2 and -6 mm day^{-1}. Over the aforementioned topographic peaks, negative

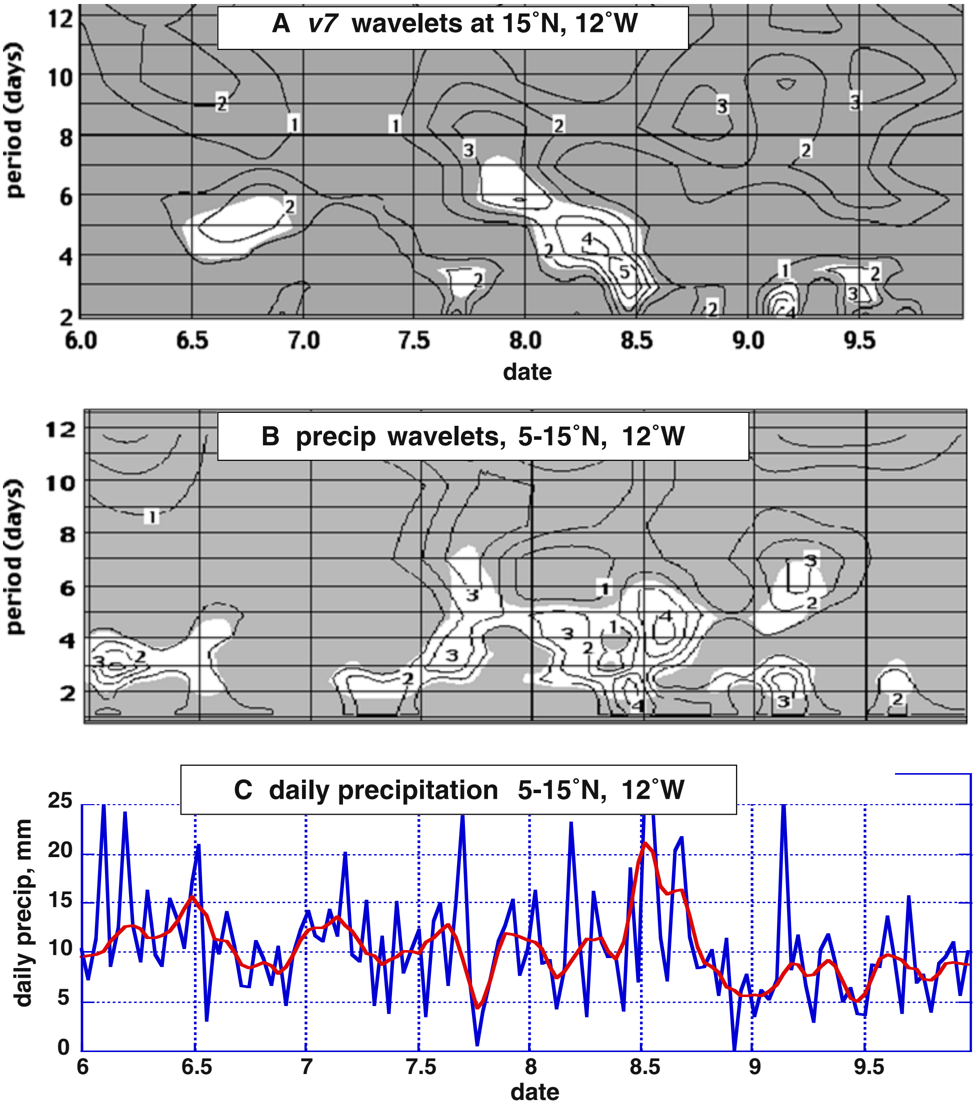

Fig. 17 **a** Wavelet amplitudes of the *v7* time series at 15°N, 12°W for JJAS 2002, **b** wavelet amplitudes of the JJAS precipitation time series for 5–15°N, 12°W, **c** time series of daily precipitation along 12°W, averaged over 5–15°N (*blue*) and a smoothed fit to the time series (*red*). *White areas* in **a** and **b** indicate amplitudes that are statistically significant at the 95% confidence level

precipitation errors became more extreme by about -2 mm day^{-1}.

Figure 20c is the Hovmöller time–longitude distribution of daily precipitation rates averaged between 5 and 15°N for July 31–August 23, 1998 for the smoothed topography experiment. Figure 20c can be compared to the corresponding TRMM estimates, shown in Fig. 8a, and results for the parallel simulation with the original orography that are shown in Fig. 8b. The impact of the low-resolution orography on these daily precipitation rates was a reduction of up to 5 mm day^{-1}. However, the time–space correlation between modeled and TRMM rainfall seems not to have been adversely affected. Moreover, the frequency of rates between 0 and 2 mm day^{-1} was increased so that the low-resolution topography results slightly improve the definition of the no-rain and light-rain intervals between rain events. These results hold for the rest of the 1998 summer and for a similar test made for a second season.

5 Discussion and conclusion

A 6-year data set of the summer climate on a 0.5° grid over West Africa, the adjacent Atlantic Ocean and Gulf of Guinea was created. The three-dimensional distributions of climate variables derive from simulations by a limited area model, the RM3, driven by NCPR data as LBCs, in effect, dynamic downscaling NCPR data sets. Observed (NCPR) SSTs were used as the maritime lower boundary condition.

The structure of the 6-year mean RM3 zonal circulation resembles NCPR, but there are disagreements regarding AEJ core speeds and the strength of maximum monsoon westerlies in the mean and for particular years. RM3 ground and surface air temperatures were several degrees too low over the Sahara maximum, but were slightly more realistic than NCPR along the Gulf of Guinea coast, compared with CRU analyses interpolated from station observations.

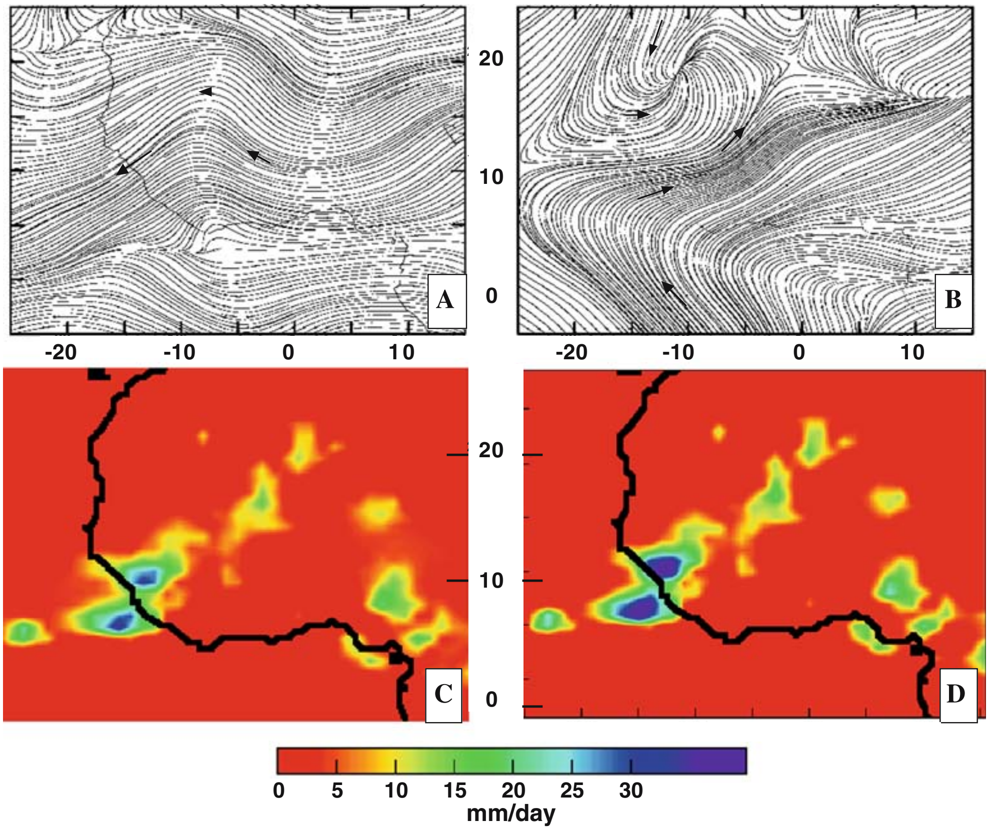

Fig. 18 **a** RM3 700 mb circulation, 00 UT on August 3, 2002, **b** RM3 925 mb circulation, 00 UT, August 3, 2002, **c** RM3 August 2, 2002 precipitation rates (mm day^{-1}), **d** TRMM August 2, 2002 precipitation rates (mm day^{-1}) (Courtesy of DAAC/GSFC)

TRMM estimates of precipitation rates are based on a combination of remote (satellite) radiometric observations from infra-red, microwave and radar instrumentation. RM3, on the other hand, computes precipitation rates based on parameterizations that depend on the model-generated evolution of the three-dimensional circulation, temperature and humidity distributions. Neither system has information from rain gauge measurements. Accordingly, it is very encouraging that many aspects of the precipitation regime produced by each of these two methods are in agreement. Six-year mean RM3 summer precipitation rates are quite consistent with corresponding TRMM estimates, although the RM3 produces a lower frequency of rates below 2 mm day^{-1} and fewer extreme maxima. Comparisons with (CRU) seasonal mean precipitation rates from rain gauge measurements for three of the overlapping seasons sustains the credibility of both RM3 and TRMM estimates. RM3 and TRMM daily precipitation estimates show a previously reported northward jump of high rates over West Africa in early July as well as the gradual southward retreat of the rain band between August and late September. RM3 and TRMM representations of the 6-year mean time–latitude distribution of daily precipitation over West Africa are remarkably similar, even matching the timing of breaks in heavy rain and some of the dates of very rainy episodes.

The study demonstrates that the RM3 accurately produces the actual space-time distribution of daily precipitation by processing the input of "observed" climate data four times daily along the lateral boundaries. The respective patterns of TRMM and RM3 westward propagating AWD precipitation "footprints" on JJAS time–longitude Hovmöller diagrams (of daily precipitation rates) show a remarkable congruence. Correlation coefficients were as high as 0.90 for three JJAS seasons, and averaged 0.88 for the six seasons considered here. Additionally, a significantly high correlation was found between the time series of daily precipitation during one summer from the average of 34 rain gauges near Niamey versus the corresponding RM3 simulation and TRMM data. These favorable results are particularly encouraging in light of the recognized challenges in modeling warm season rainfall (Fritch and Carbone 2004). Diagonal rainfall swaths on the Hovmöller plots were often closely related to westward moving areas of low-level convergence, and sometimes to the periodic waves implied by the spectral analysis and/or to upper tropospheric divergence. The space-time distributions of precipitation rates produced by the NCPR do not form westward propagating bands that match TRMM or RM3. A sensitivity experiment in which the RM3 terrain heights were replaced by the lower-resolution NCPR orography featured more extreme negative precipitation errors, but the formation and propagation of precipitation bands was not compromised. Results imply that the NCPR deficiencies relative to the RM3 are more closely related to the relative performance of the models' dif-

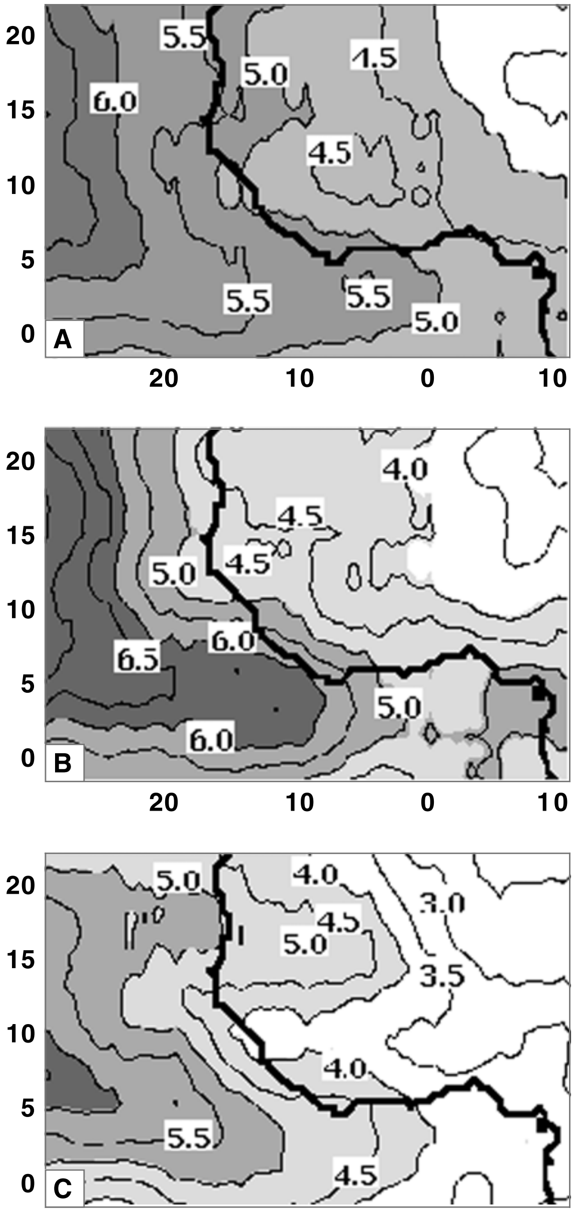

Fig. 19 Spatial distribution of average spectral amplitudes between 3 and 6-day periods for *v7* JJAS time series. **a** Average for 1998–2003, **b** for 1999, **c** for 2003

ferent moist convection parameterizations as they are applied at the different horizontal grid resolutions.

The six RM3 JJAS simulations showed noticeable interannual variability in precipitation rates. RM3 daily precipitation rate maxima were usually lower than for TRMM. RM3 seasonal and August precipitation anomaly patterns, relative to 6-year means, agreed with corresponding TRMM anomaly patterns over some areas, but there were noticeable discrepancies. For example, RM3 positive rainfall anomalies for JJAS 2002, were not consistent with TRMM data over most of West Africa. Since the magnitude of seasonal precipitation anomalies is often a small fraction of the total rainfall, anomaly spatial patterns in the two data sets are more challenging to match than the patterns of precipitation rates.

Spectra of RM3 700 mb meridional wind (*v7*) time series show peaks for 3 to 6-day periods over certain areas of the model domain. At any particular location, the exact period of each spectral peak varies from season to season. For example, each of the six seasonal *v7* simulations at 15°N, 12°W experienced at least one spectral peak in the 3 to 6-day period interval. The periodicity represented by these peaks is related to easterly waves, called here AWD, and many of them are associated with significant rainfall. Wavelet analysis showed that distinct periodic behavior of *v7* is apt to wax and wane throughout the summer. Precipitation time series also exhibit spectral peaks at 4 to 5-day periods. However, results indicate that weeks with more organized AWD activity are not necessarily rainier than weeks with lulls in AWD, probably because these disturbances are not the exclusive precipitation trigger. On the other hand, the AWD shown for August 2–3, 2002 *was* responsible for significant precipitation. The system included a near-surface closed cyclonic circulation west of the 700 mb trough, the center of which was rather dry. Heavy rainfall in fact occurred below the western flank of the upper wave, imbedded within low-level westerly and southerly moisture advection well to the south of the surface cyclone center. Spatial distributions of 3 to 6-day period spectral amplitudes of *v7* time series show regional maxima, but their locations vary from year to year. Two of the more common maxima are along 17°N and along 4°N. These maxima indicate the locations where 3 to 6-day periodicity of *v7* is either very strong or very frequent, hence, locations with significant AWD activity. The AWD example for August 2–3, 2002 includes a distinct wave crest near 17°N and a cyclonic circulation discontinuity at 4°N, consistent with the aforementioned analyzed spatial patterns of spectral amplitude maxima.

The documented advantages of RM3 simulated precipitation simulations over the NCPR product presumably result in part from the higher spatial resolution of the RM3, suggesting that it better simulates mesoscale convergence centers related to the time–space distribution of precipitation. The timing of mid-tropospheric waves in these RM3 simulations correlates well with their timing in NCPR data, as evidenced by the very high correlation coefficients between the corresponding time series of the meridional wind component at 700 mb (*v7*). However, RM3 *v7* fluctuations have a consistently smaller range than NCPR *v7* time series, implying that the RM3 AWDs have lower amplitudes. Preliminary experiments indicated that increasing the model's vertical resolution to 28 layers could produce wider ranging fluctuations of *v7*.

RM3 seasonal mean near-surface meridional winds are also weaker than corresponding NCPR values within the monsoon air mass over West Africa. The northward advance of monsoon air is driven by the meridional temperature gradient, which Fig. 3 shows was too weak

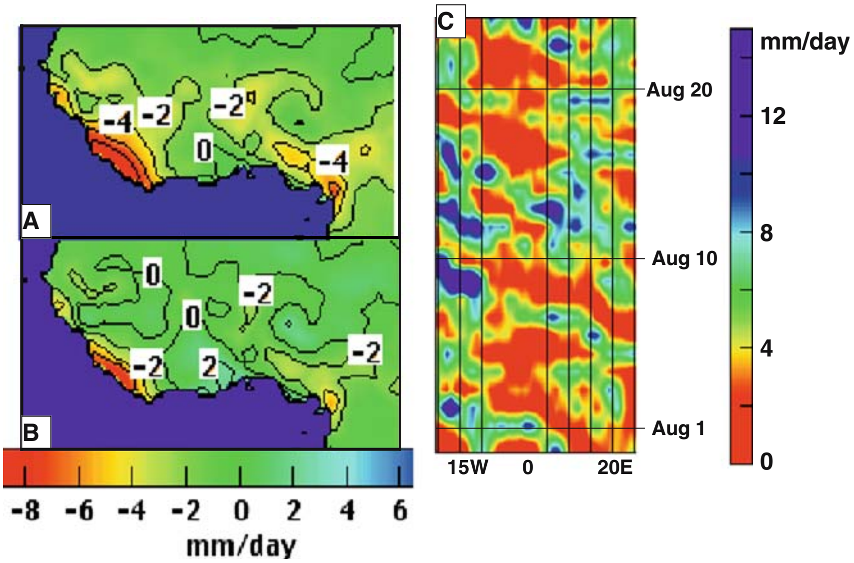

Fig. 20 **a** JJAS 1998 precipitation rate errors (mm day^{-1}) relative to CRU observations (Courtesy of East Anglia University) for RM3 simulation using NCPR orography, **b** JJAS 1998 precipitation rate errors (mm day^{-1}) relative to CRU observations (Courtesy of East Anglia University) for RM3 simulation using 0.5° resolved orography, **c** time–longitude distribution of daily precipitation rates between July 31 and August 23, 1998, averaged over 5–15°N, for RM3 simulation with NCPR orography

in the RM3 simulations. Perhaps future modeling improvements that will succeed in tightening the meridional temperature gradient will concomitantly improve this aspect of the modeled circulation.

The RM3's realistic simulation of observed time–space distributions of precipitation rates signifies that this product of dynamic downscaling of NCPR provides a realistic three-dimensional data set of climate evolution over West Africa during JJAS 1998–2003. Results show that the RM3 could be a valuable tool for sensitivity experiments that contribute to our understanding of the physical mechanisms underlying the variability of the West African monsoon. The evaluation also implies that the RM3 would provide credible spatial detail by downscaling high quality GCM seasonal climate predictions or projections of decadal climate change. These applications will be pursued in tandem with the incorporation of additional model improvements.

Acknowledgements The research was supported by the National Science Foundation grant no. ATM-0354589 and by the NASA Climate and Earth Observing System Programs. The authors gratefully acknowledge the assistance and participation of Gil Zamfirescu and Charles Sosa in processing some of the data for the study. The very helpful suggestions of three anonymous reviewers are also gratefully acknowledged.

References

Beven KJ, Kirkby MJ (1979) A physically-based variable contributing area model of basin hydrology. Hydrol Sci J 24:43–69

Burpee R (1972) The origin and structure of easterly waves in the lower troposphere of North Africa. J Atmos Sci 29:77–90

De Ela R, Laprise R, Denis B (2002) Forecasting skill limits of nested, limited-area models: a perfect-model approach. Mon Wea Rev 130:2006–2023

Del Genio A, Yao M-S (1993) Efficient cumulus parameterization for long-term climate studies. The GISS scheme. In: Emanuel K, Raymond D (eds) Cumulus parameterization, vol 24. American Meteorological Society Monograph Series, Boston, pp 181–184

Del Genio A, Yao M-S, Kovari W, Lo K-W (1996) A prognostic cloud water parameterization for global climate models. J Clim 9:270–304

Denis B, Laprise R, Caya D, Coté J (2002) Downscaling ability of one-way nested regional climate models: the Big-Brother experiment. Clim Dyn 18:627–646

Diedhiou A, Janicot S, Viltard A, de Felice P, Laurent H (1999) Easterly wave regimes and associated convection over West Africa and tropical Atlantic: results from NCEP/NCAR and ECMWF reanalyses. Clim Dyn 15:795–822

Druyan L, Fulakeza M, Thiaw W (2000) Regional model simulations of African wave disturbances. JGR 105:7231–7255

Druyan L, Hall T (1996) The sensitivity of African wave disturbances to remote forcing. J Appl Meteorol 35:1100–1110

Druyan L, Lonergan P, Saloum M (1996) African wave disturbances and precipitation at Niamey during July–August, 1987 and 1988. Clim Res 7:71–83

Druyan L, Lonergan P, Cohen J (1997) Case studies of African wave disturbances in gridded analyses. Mon Wea Rev 125:2520–2530

Druyan L (1998) The role of synoptic systems in the interannual variability of Sahel rainfall. Meteorol Atmos Phys 65:55–75

Druyan L, Fulakeza M, Lonergan P, Saloum M (2001) A regional model study of synoptic features over West Africa. Mon Wea Rev 129:1564–1577

Druyan L, Fulakeza M, Lonergan P (2004) Land surface influences on the West African summer monsoon: implications for synoptic disturbances. Meteorol Atmos Phys 86:261–273

Druyan L, Fulakeza M (2005) Mesoscale climate analysis over West Africa. CLIVAR Exch 34(3):20–35

Duvel JP (1990) Convection over tropical Africa and the Atlantic Ocean during northern summer. Part II: Modulation by easterly waves. Mon Wea Rev 118:1855–1868

Fortune M (1980) Properties of African squall lines inferred from time-lapse satellite imagery. Mon Wea Rev 108:153–168

Fritsch M, Carbone R (2004) Improving quantitative precipitation forecasts in the warm season. Bull Am Meterol Soc 85:955–965

Gibson JK, Kallberg P, Uppala S, Hernandez A, Nomura A, Serrano E (1997) ECMWF reanalysis project report series, part I ERA description. ECMWF, Reading, p 72

Giorgi F, Bates G, Nieman S (1993) The multiyear surface climatology of a regional atmospheric model over the Western United States. J Clim 6:75–95

Giorgi F, Marinucci M (1996) An investigation of the sensitivity of simulated precipitation to model resolution and its implication for climate studies. Mon Wea Rev 124:148–166

Grist J, Nicholson S (2001) A study of the dynamic factors influencing the rainfall variability in the West African Sahel. J Clim 14:1337–1359

Hansen J et al (2002) Climate forcings in Goddard Institute for Space Studies SI2000 simulations. JGR DOI: 10.1029/200IJD001143

Huffman GJ, Adler RF, Arkin P, Chang A, Ferraro R, Gruber A, Janowiak J, McNab A, Rudolph B, Schneider U (1997) The global precipitation climatology project (GPCP) combined precipitation dataset. Bull Am Meterol Soc 78:5–20

Kistler R et al (2001) The NCEP-NCAR 50-year reanalysis: monthly means CD-ROM and documentation. Bull Am Meterol Soc 82:247–267

Lamb P, Peppler R (1991) West Africa. In: Glantz MH, Katz RW, Nicholls N (eds) Teleconnections: linkages between ENSO, worldwide climate anomalies, and societal impacts. Cambridge University Press, London, pp 121–189

Landsea C, Gray W (1992) The strong association between western Sahelian monsoon rainfall and intense Atlantic hurricanes. J Clim 5:435–453

Lau W, Matsumoto J, Bollasina M, Berbery H (2004) Diurnal variability in the monsoon region: preliminary results from the CEOP inter-monsoon studies (CIMS). CEOP Newsl 5:2–4

Leung L, Qian Y, Bian X (2003) Hydroclimate of the western US based on observations and regional climate simulation of 1981–2000. Part I: Seasonal statistics. J Clim 16:1892–1911

Leung L, Qian Y, Bian X, Washington W, Han J, Roads J (2004) Mid-century ensemble regional climate change scenarios for the western US. Clim Change 62:75–113

Moustaoui M, Royer J-F, Chauvin F (2002) African easterly wave activity in a variable resolution GCM. Clim Dyn 19:289–301

Matthews E (1983) Global vegetation and land use: new high-resolution data bases for climate studies. J Clim Appl Meteorol 22:475–487

Matthews E (1984) Prescription of land-surface boundary conditions in GISS GCM II: a simple method based on high-resolution vegetation data bases. NASA Tech. Memo 86096. GSFC, Greenbelt, p 20

New M, Lister D, Hulme M, Makin I (2002) A high-resolution data set of surface climate over global land areas. Clim Res 21:1–25

Norquist D, Recker E, Reed R (1977) The energetics of African wave disturbances as observed during Phase III of GATE. Mon Wea Rev 105:334–342

Pytharoulis I, Thorncroft C (1999) The low-level structure of African easterly waves in 1995. Mon Wea Rev 127:2266–2280

Reed R, Norquist D, Recker E (1977) The structure and properties of African wave disturbances as observed during Phase III of GATE. Mon Wea Rev 105:317–333

Reed R, Klinker E, Hollingsworth A (1988) The structure and characteristics of African easterly wave disturbances as determined from the ECMWF operational analysis/forecast system. Meteorol Atmos Phys 38:22–33

Rosenzweig C, Abramopoulos F (1997) Land-surface model development for the GISS GCM. J Clim 10:2040–2054

Sultan J, Janicot S (2000) Abrupt shift of the ITCZ over West Africa and intraseasonal variability. Geophys Res Lett 27:3353–3356

Taleb E-H, Druyan L (2003) Relationships between rainfall and West African wave disturbances in station observations. Int J Climatol 23:305–313

Thorncroft C, Blackburn M (1999) Maintenance of the African easterly jet. Q J R Meteorol Soc 125:763–786

Thorncroft C, Hodges K (2001) African easterly wave variability and its relationship to Atlantic tropical cyclone activity. J Clim 14:1166–1179

Thorncroft C et al (2003) The JET2000 Project: Aircraft observations of the African Easterly Jet and African easterly waves. Bull Am Meterol Soc 84:337–351

Torrence C, Compo G (1998) A practical guide to wavelet analysis. Bull Am Meterol Soc 79:61–78

Uppala SM et al (2005) The ERA-40 re-analysis. Q J R Meteorol Soc 131:2961–3012

Ward MN et al (2004) Seasonal-to-decadal predictability of West Africa climate. CLIVAR Exch 9(14):19–20

Xue Y, Shukla J (1993) The influence of land surface properties on Sahel climate. Part I: Desertification. J Clim 6:2232–2245